SIMULATION OF THE STABILIZATION OF MAGNETIC ISLANDS BY ECRH AND ECCD

A THESIS SUBMITTED TO
THE GRADUATE SCHOOL OF NATURAL AND APPLIED SCIENCES
OF
MIDDLE EAST TECHNICAL UNIVERSITY

BY

BİRCAN AYTEN

IN PARTIAL FULFILLMENT OF REQUIREMENTS
FOR
THE DEGREE OF MASTER OF SCIENCE
IN
PHYSICS

SEPTEMBER 2009

Approval of the thesis:

SIMULATION OF THE STABILIZATION OF MAGNETIC ISLANDS BY ECRH AND ECCD

submitted by **BİRCAN AYTEN** in partial fulfillment of the requirements for the degree of **Master of Science in Physics Department, Middle East Technical University** by,

Prof.Dr. Canan Özgen _____
Dean, Graduate School of **Natural and Applied Sciences**

Prof. Dr. Sinan Bilikmen _____
Head of Department, **Physics**

Prof. Dr. Sinan Bilikmen _____
Supervisor, **Physics Dept., METU**

Dr. Egbert Westerhof _____
Co-Supervisor, **Tokamak Physics Group, FOM Institute**

Examining Committee Members:

Prof. Dr. Ramazan Aydın _____
Physics Dept., Atılım University

Prof. Dr. Sinan Bilikmen _____
Physics Dept., METU

Assist. Prof. Dr. Hakan Altan _____
Physics Dept., METU

Dr. Halil Berberoğlu _____
Physics Dept., METU

Dr. Demiral Akbar _____
Physics Dept., METU

Date: 28.09.2009

I hereby declare that all information in this document has been obtained and presented in accordance with academic rules and ethical conduct. I also declare that, as required by these rules and conduct, I have fully cited and referenced all material and results that are not orginal to this work.

Name, Last name : Bircan Ayten

Signature :

ABSTRACT

SIMULATION OF THE STABILIZATION OF MAGNETIC ISLANDS BY ECRH AND ECCD

AYTEN, BİRCAN

MS.,Department of Physics

Supervisor: Prof. Dr. Sinan Bilikmen

Co-Supervisor: Dr. Egbert Westerhof

September 2009, 57 pages

An almost universal instability in high pressure plasmas is the Neoclassical Tearing Mode (NTM). NTMs are driven by local perturbations in the current density and result in magnetic island like deformations of the magnetic topology. They can be stabilized by compensating the current perturbations with local electron cyclotron resonance heating (ECRH) or with non-inductive current drive (ECCD). The modified Rutherford equation describes the nonlinear evolution of tearing modes as determined by various contributions to the local current density pertubation. An extensive investigation of the two terms representing the stabilizing effects from ECRH and ECCD have been made resulting in accurate description of both

terms. The results of this model can now be compared to the experimental observations. For this purpose, an extensive data set exists from the past experiments on tearing mode stabilization by ECRH and ECCD on TEXTOR. The properly benchmarked model can then be used to predict the effectiveness of ECRH and ECCD for NTM stabilization on International Thermonuclear Experimental Reactor (ITER). In addition, a number of predictions on the effects of ECRH and ECCD on the growth of the NTM have been made on the basis of crude approximations to the ECRH and ECCD tems in the modified Rutherford equation. These predictions can now be checked against the more accurate expressions obtained.

Keywords: Tokamak Physics, MHD Instabilities

ÖZ

MANYETİK ADALARIN ECRH VE ECCD YÖNTEMLERİYLE KARARLI HALE GETİRİLMESİNİN SİMULASYONU

AYTEN, BİRCAN

Yüksek Lisans, Fizik Bölümü

Tez Yöneticisi: Prof. Dr. Sinan Bilikmen

Ortak Tez Yöneticisi: Dr. Egbert Westerhof

Eylül 2009, 57 sayfa

Neoclassical tearing mode (NTM) hemen hemen bütün yüksek basınçlı plazmalarda görülen evrensel bir kararsızlıktır. Akım yoğunluğundaki tedirginlikten oluşup manyetik topolojide manyetik adalara benzeyen deformasyonlara neden olurlar. Akım tedirginlikleri ECRH (Electron cyclotron resonance heating) ve ECCD (Non-inductive current drive) yöntemleriyle eşitlenerek kararlı hale getirilebilirler. Düzeltilmiş Rutherford denklemi tearing mode kararsızlıklarının lineer olmayan oluşumlarını açıklar. Bu denklemdeki ECRH ve ECCD terimlerinin kararlı hale getirmedeki etkileri üzerine yaplan büyük çaplı araştırmalar bu terimlerin kesin bir şekilde

tanımlanmalarına neden olmuştur. Şimdi ise bu modelin sonuçlar deneysel gözlemlerle karşılaştırılacaktır. Bu amaçla, bu konu hakkında TEXTOR Tokamak'ından geçmiş deneylerde geniş çaplı veri elde edilmiştir. Uygun şekilde yapılmış olan karşılaştırılmış model, ITER (Uluslararası Termonükleer Deneysel Reaktör) üzerinde ECRH ve ECCD yöntemlerinin NTMleri kararlı hale getirmekteki etkinliklerini tahmin etmekte kullanılacaktır. Bunun yanı sıra, ECRH ve ECCD nin bu kararsızlıkların oluşumundaki etkileri üzerine, düzeltilmiş Rutherford denklemine dayanılarak, kabaca yapılmış olan tahminler de kontrol edilecektir.

Anahtar Kelimeler: Tokamak Fiziği, MHD Kararsızlıkları

To my family

ACKNOWLEDGEMENTS

First of all, I would like to thank Prof.Dr. Sinan Bilikmen for giving me the chance to pursue my dreams. I am grateful to Dr. Egbert Westerhof for his valuable guidance, corrections and discussions. I also would like to acknowledge Diego De Lazzari for his daily supervision. It is a pleasure to thank Marco de Baar and Waldo Bongers who made this thesis possible. Finally, I would like to show my gratitude to my family for their love and encouragement.

TABLE OF CONTENTS

LIST OF TABLES

LIST OF FIGURES

CHAPTER 1

INTRODUCTION

In nuclear fusion the lighter nuclei merge to form a heavier nucleus. It is the energy source of our universe as all the stars and the sun are powered by this type of reaction. In most of the cases the total mass of the reactants is larger than the mass of the product in most of the cases. This mass difference accounts for the energy released according to Einstein's energy-mass relation $E = \Delta m \cdot c^2$.

For the controlled fusion on Earth the reaction between two hydrogen isotopes deuterium and tritium, shown in Figure 1.1, is the most promising candidate as it has the largest cross section at lower energies among all the possible reactions. The reaction produces a helium nucleus (α particle) and a neutron. It has a mass defect $\Delta m = m_D + m_T - (m_{He} + m_n) = 3.1 \times 10^{-29}$ kg. The released energy is distributed into these two product particles inversely proportional to their masses. The neutron receives 14.1 MeV in the form of kinetic energy whereas the α particle has 3.5 MeV.

$$D + T \rightarrow He + n + 17.6\ MeV \tag{1.1}$$

Fusion fuels (D and T) are sufficiently abundant. Deuterium exists in the oceans. Tritium is an unstable radioactive isotope yet it can be produced by a nuclear reaction of the neutrons from the D-T reaction and lithium. The latter is also very abundant in the Earth's crust.

This fusion reaction does not occur spontaneously. Since both deuterium

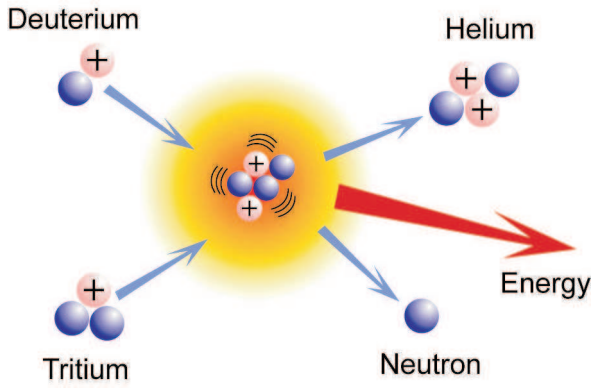

Figure 1.1:
Fusion reaction between two hydrogen isotopes, deuterium and tritium. The products are a 3.5 MeV α particle and 14.1 MeV neutron.

and tritium have positively charged nuclei, they feel repulsive Coulomb force preventing them from fusing. This Coulomb barrier can be overcome by increasing the temperature of the reacting gases to about 10 keV (1 eV=11600 K). At these high thermal energies the mixture of deuterium and tritium gases are completely ionized and become a plasma composed of charged ions and electrons.

1.1 Ignition

One of the aims of the thermonuclear fusion research is to achieve a self sustaining plasma to be recognized as an energy producing system. By a self sustaining plasma an ignited plasma is meant where all energy losses are compensated by the energy of the α particles. These particles transfer their energy to the plasma by collisions while slowing down. The necessary condition for the deuterium-tritium reaction to realize a self sustaining plasma is expressed by the triple product of density n, energy confinement

time τ_E and temperature T [2] [16]:

$$nT\tau_E \geq 5 \times 10^{21} m^{-3}\ s\ keV \tag{1.2}$$

It is called the Lawson criterion and $1/\tau_E$ is the rate at which plasma loses its energy. A fusion reaction is self-sustained provided that at around 10 keV the density and energy confinement time are sufficiently high. There are different ways to achieve these requirements [18]. One of them is confining the plasma by making use of magnetic fields (magnetic confinement). Second type of confinement is laser- or beam- induced inertial confinement. In this thesis only magnetically confined plasmas will be discussed.

1.2 Tokamak

A plasma can be confined by magnetic fields since it is composed of electrically charged nuclei and electrons. The motion of these particles in response to a magnetic field is dictated by the Lorentz force $\vec{F} = q\vec{u} \times \vec{B}$. Although electrons and ions can freely move along the field lines, their motion perpendicular to the field lines is restricted to gyrate around these lines with cyclotron frequency $\omega_c = qB/m$ and a gyroradius (Larmor radius) $\rho_L = u_\perp/\omega_c$, where B is the magnetic field, q the charge of the particle, m the mass of the particle and $u_\perp$ the magnitude of the particle velocity perpendicular to the magnetic field (see Figure 1.2).

That the motion parallel to the magnetic field lines is not restricted results in particle losses from the plasma in linear configurations (end losses). Consequently, the required energy confinement time τ_E can not be reached. The most effective confinement of high temperature plasmas is achieved when the magnetic field lines close themselves inside the plasma forming a toroidal geometry.

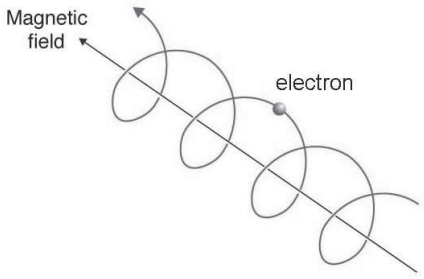

Figure 1.2: An electron gyrating around a magnetic field line.

The curvature and gradient of this purely toroidal magnetic field lead to a vertical drift which is in opposite directions for electrons and ions. This charge separation generates a vertical electric field and this electric field in turn induces an outward radial $\vec{E} \times \vec{B}$ drift of the whole plasma which is independent of the charge of the particles as shown in Figure 1.3.

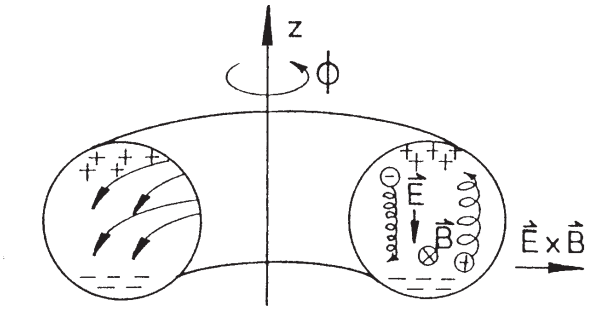

Figure 1.3:
Vertical drifts and outward particle drift due to $\vec{E} \times \vec{B}$ drift in a purely toroidal geometry.

Thus, a pure toroidal magnetic field is not enough to confine the plasma effectively. In order to avoid such radial losses of electrons and ions a poloidal magnetic field should be introduced. As a result, a helical magnetic field is formed.

There are different approaches for the introduction of the poloidal magnetic field, B_θ. In a *stellarator* the helical field is generated by external coils wound around the plasma torus. In a *tokamak* toroidal component of the magnetic field B_ϕ is produced by poloidal currents in the external coils (see Figure 1.4).

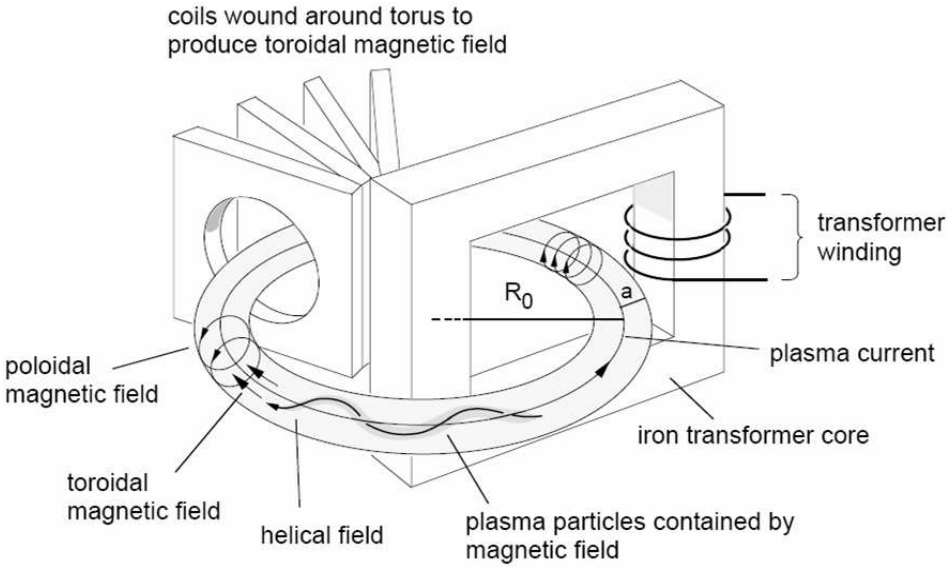

Figure 1.4:
A schematic representation of a tokamak. The major and minor radius are indicated by R_0 and a, respectively. Toroidal magnetic field produced by poloidal currents in the external coils and poloidal magnetic field generated by a toroidal current I_p form the helical field.

Its poloidal magnetic field is produced by a toroidal current I_p in the plasma which is induced making the plasma the secondary winding of a transformer. This current also participates in plasma formation and heating. Among all the magnetic configurations invented so far, best performance has been achieved by the tokamak. Its name is an acronym for the Russian name *TOroidalnaya KAmera i MAgnitnaya KAtushka* which means toroidal chamber with magnetic coils.

1.3 TEXTOR

In this research experimental data from TEXTOR tokamak are used. TEXTOR (Tokamak Experiment for Technology Oriented Research) is a medium sized, circular, limiter tokamak with major radius $R_0 = 1.75$ m and minor radius $a = 0.47$ m. The toroidal magnetic field is generated by a set of 16 coils around the vacuum vessel and this field can go up to 3 T. Plasma current is produced by the iron transformer core and its value can be 800 kA maximum. However, TEXTOR is typically operated with a toroidal field $B_\phi = 2.25$ T and plasma current $I_p = 400$ kA. A discharge can last up to 10 s maximum but its typical value is 6 s. The main parameters of TEXTOR are listed in the Table 1.1.

1.3.1 Plasma Heating

The plasma current I_p is the primary source for heating for all tokamaks. The power dissipated by the flow of this current is called the Ohmic heating power. The contribution of this Ohmic heating is given by ηJ^2, where η is the low but finite resistivity of a high temperature plasma. Note that this plasma resistivity is proportional to $T_e^{-3/2}$. So, as the temperature increases, Ohmic heating power decreases. Moreover, the maximum value

Table 1.1: TEXTOR parameters.

Major radius R_0	1.75 m
Minor radius a	0.46 m
Plasma volume	7 m^3
Toroidal field B_ϕ	< 3 T
Plasma current I_p	< 0.8 MA
Pulse length	< 10 s
Ohmic power	0.3-0.5 MW
Installed heating power (ECRH + ICRH + NBI)	9 MW
ECCD	< 50 kA
Typical Electron and Ion temperature on axis	1.2 keV
Typical electron density on axis	$3 \cdot 10^{19} m^{-3}$

of plasma current is restricted by the occurrence of magnetohydrodynamic instabilities. Therefore, the Ohmic heating itself is not sufficient to provide the necessary temperature to initiate a fusion reaction and keep the plasma burning. In TEXTOR its power ranges between 0.3 and 0.5 MW. Thus, additional heating methods are necessary to be employed. In TEXTOR there are two additional ways of heating the plasma (increasing the energy of the plasma). First way is to inject highly energetic particles inside the plasma. This method is called **neutral beam injection (NBI)**.

In neutral beam injectors a beam of ionized particles are accelerated to a high energy and neutralized. This neutral beam is injected into the plasma. While penetrating into the plasma, the neutral particles are ionized by charge exchange reactions with the plasma ions. Then they transfer

their energy and momentum to plasma electrons and ions through collisions. On TEXTOR there are two tangential neutral beam injectors [2] [12] installed. Each can deliver a maximum of 1.5 MW heating power of neutrals at energies up to 60 keV. The typical neutral particles are H, D and He.

Second way is to inject electromagnetic energy inside the plasma. The power of the electromagnetic waves is absorbed either by the ions or the electrons through resonant interaction with their cyclotron motion (or their harmonics). This way of heating the plasma is called **Ion Cyclotron Resonance Heating (ICRH)** or **Electron Cyclotron Resonance Heating (ECRH)**, respectively. ICRH frequencies are much lower than ECRH frequencies since ion mass is much larger than the electron mass. Therefore ECRH wavelength is smaller (around 2 mm) [2]. This property of ECRH provides accurate localization of the heating power and driven current as in the case of stabilization of magnetic islands.

On TEXTOR there are two sets of two ICRH antennae [2] installed on the low field side of the tokamak. Each set can generate waves with frequencies between 25 and 38 MHz injecting power of 2 MW. Continuous power injection can last up to 3 seconds.

For ECRH power on TEXTOR there are two gyrotrons [12], a 110 GHz, 350 kW, 200 ms gyrotron and a 140 GHz, 850 kW, 10 s gyrotron. They generate extra-ordinary polarization mode (X-mode) microwaves to be absorbed in the plasma at the second harmonic of the electron cyclotron resonance.

By rotating the mirror of the launcher around its vertical axis, a variation in the radial position of ECRH power deposition is obtained while rotation around its horizontal axis leads to Electron Cyclotron Current Drive (ECCD).

1.3.2 Dynamic Ergodic Divertor

Dynamic Ergodic Divertor (DED) [4] is a tool installed at TEXTOR. It is composed of 16 perturbation coils and 2 more compensation coils installed at the inboard side (high field side) of TEXTOR, see Figure 1.5. These 16 perturbation coils run helically around the torus being aligned to the magnetic field lines at $q = 3$ surface. By applying current to these perturbation coils a magnetic field perturbation is obtained. The two compensation coils, above and below the perturbation coils, are used to reduce the stray field.

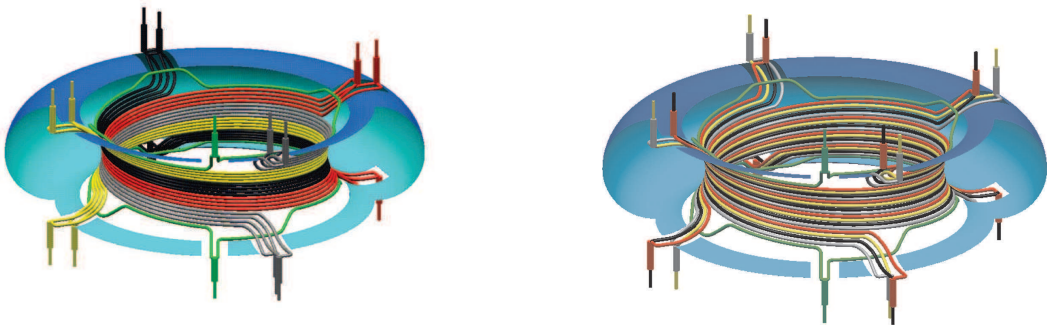

Figure 1.5:
The DED coil configurations for the 3/1 (left hand side) and 12/4 (right hand side) operation modes. The 16 helical perturbation coils (black, yellow, gray and red) are located at the inboard side of the vacuum vessel (high field side). Coils fed by different phased currents are indicated by the different colors. The green coils above and below the perturbation coils are the compensation coils.

The coils can either be fed with direct or alternating current (DC or AC) with an amplitude of up to 15 kA each. DC mode generates a static magnetic perturbation whereas a rotating (dynamic) magnetic field pertur-

bation is obtained in AC mode operation since in this mode the phase of each coil changes. In AC mode the 16 coils can be fed by four differently phased currents $(0°, 90°, 180°, 270°)$. The principal mode numbers of the perturbation fields depend on how these 16 coils are connected to these 4-phase current. There are three different operation modes (see Figure 1.5). In a 3/1 mode all coils are grouped in four sets of four coils and the coils belonging to the same group have the same phase but there is a 90° phase shift between the neighboring group of coils. In a 12/4 mode there is a 90° phase difference between the neighboring coils. In a 6/2 mode which is an operational mode between 3/1 and 12/4. It has groups consisting of 2 coils. The coils in each group have the same phase while the next group have 90° phase shift.

AC mode is divided into two categories with respect to phase change as time passes [2]. If the phase increases, it is called AC^+ mode. The resulting field rotates counterclockwise in the poloidal direction and clockwise in the toroidal direction. The phase decreases in AC^- mode and the field rotates toroidally counterclockwise and poloidally clockwise. The AC current frequencies range from 0 to 10 kHz but typically frequencies 1 kHz and 3.75 kHz are chosen.

CHAPTER 2

THEORY OF NEOCLASSICAL TEARING MODES

2.1 Magnetohydrodynamics

Magnetohydrodynamics (MHD) provides a single fluid description of plasma behavior. It differs from the kinetic theory description of plasmas in the sense that the dynamics of electrons and ions are not treated separately. Below are the simplified MHD equations [16] [1] [7] to be used in this research.

Continuity equation:

$$\frac{\partial \rho}{\partial t} + \vec{\nabla}.(\rho \vec{v}) = 0 \tag{2.1}$$

Equation of motion:

$$\rho \frac{\mathrm{d}\vec{v}}{\mathrm{d}t} = \vec{J} \times \vec{B} - \vec{\nabla} p \tag{2.2}$$

where the right hand side is the force density acting on a fluid element. The term on the left hand side is the inertial force and the first and the second term on the right hand side are the magnetic force and the pressure gradient force, respectively.

Equation of energy:

$$\frac{\mathrm{d}(p\rho^{-\gamma})}{\mathrm{d}t} = 0 \tag{2.3}$$

The equations above dictate the time evolution of mass, momentum and energy, respectively. The energy equation expresses the evolution of adiabatic fluid characterized by a ratio of specific heats, $\gamma = 5/3$.

Ampere's Law:

$$\mu_0 \vec{J} = \vec{\nabla} \times \vec{B} \tag{2.4}$$

Faraday's Law:

$$\frac{\partial \vec{B}}{\partial t} = -\vec{\nabla} \times \vec{E} \tag{2.5}$$

In the ideal MHD model the plasma is taken perfectly conducting. In this model Ohm's law implies that in a reference frame moving with the plasma the electric field is zero.

Ohm's Law (ideal):

$$\vec{E} + \vec{v} \times \vec{B} = 0 \tag{2.6}$$

The inclusion of resistivity, η in Ohm's law gives rise to the resistive MHD model.

Ohm's Law (resistive):

$$\vec{E} + \vec{v} \times \vec{B} = \eta \vec{J} \tag{2.7}$$

Note that the displacement current in Maxwell's equations is neglected.

2.2 Resistivity

Neoclassical resistivity of a fully ionized toroidal plasma is given as [16]:

$$\eta \approx 2.8 \cdot 10^{-8} \frac{Z_{eff}}{T_e^{3/2}} (1 - \varepsilon^{1/2})^{-2}. \tag{2.8}$$

Assuming that electric field is constant throughout the plasma and neoclassical effects can be neglected, Ohm's law gives the current density profile as [14]

$$J_{\parallel} = k_s T_e^{3/2}(r), \tag{2.9}$$

where k_s depends on Z_{eff} which is the effective ion charge. In this research Z_{eff} is assumed to be constant, consequently k_s becomes a constant.

2.3 Magnetic surfaces

In an equilibrium ($\frac{\partial}{\partial t} = 0$) without flows ($\vec{v} = 0$), the equation of motion reduces to

$$\vec{\nabla} p = \vec{J} \times \vec{B}. \tag{2.10}$$

This force balance equation shows that a plasma can be confined by a magnetic field if the plasma pressure is balanced by a magnetic force. For a well-confined plasma which is in equilibrium, plasma pressure is maximum in the center of the poloidal cross section and independent of the toroidal angle, ϕ. For such profiles the contours of constant pressure are nested toroidal surfaces [6]. As a consequence of the equilibrium relation,

$$\vec{B} \cdot \vec{\nabla} p = 0, \tag{2.11}$$

$$\vec{J} \cdot \vec{\nabla} p = 0, \tag{2.12}$$

magnetic lines and current lines lie on surfaces of constant pressure. For that reason these constant pressure surfaces are called magnetic surfaces or flux surfaces. As can be seen from the Figure 2.1, magnetic field lines follow a helical path on their own surfaces. This helicity can be expressed by q which is called safety factor due to its importance in determining stability [16],

$$q = \frac{\triangle \phi}{2\pi}, \tag{2.13}$$

where $\triangle \phi$ is the change in the toroidal angle in a field line's trajectory to come to the same point in the poloidal cross section. In the case of a tokamak with a large aspect ratio of circular cross section, R/a, it can be approximated as [16],

$$q \simeq \frac{r B_\phi}{R B_\theta}, \tag{2.14}$$

where B_ϕ is the toroidal and B_θ is the poloidal magnetic field at a minor radius r. The safety factor, q is a flux function or surface quantity as all the field lines on the same surface have the same q value.

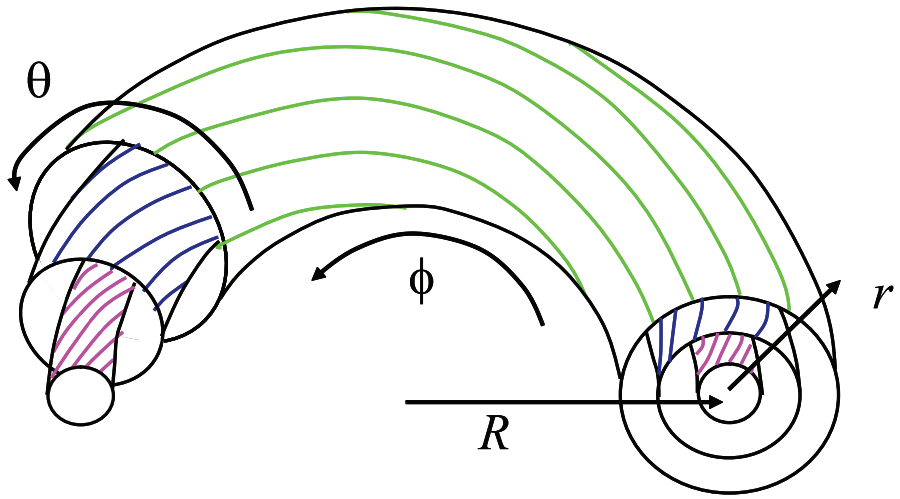

Figure 2.1: Flux surfaces in a tokamak [19].

Magnetic surfaces are divided into two categories. If a magnetic field line of a given magnetic surface closes on itself after a finite number of revolutions around the torus, then this surface is called a rational surface. The q-value of such a surface is a ratio of two integer numbers, written as m/n, where m is the poloidal and n is the toroidal mode number, meaning that the field line closes on itself after m toroidal and n poloidal turns around the torus. Instabilities often occur on rational surfaces. The second category is the so-called ergodic surfaces. The magnetic field lines cover those surfaces ergodically [6]. Magnetic axis is a closed magnetic field line and it is surrounded by the other magnetic surfaces. On this line pressure is the maximum. A measure for the efficiency of confinement is given by the ratio of plasma pressure to magnetic field pressure which is called beta, β, [16],

$$\beta = \frac{p}{B^2/2\mu_0}. \tag{2.15}$$

2.4 Magnetic islands

In the ideal configuration of magnetic field lines described above, particles and heat are well-confined. Particles gyrate around field lines. But there can occur some instabilities resulting in a change in magnetic topology. Tearing modes are one of those instabilities. They are caused by a non-axisymmetric redistribution of plasma current density and lead to a perturbed radial magnetic field on rational $q = m/n$ surfaces resonant with that perturbation. This perturbation breaks and reconnects magnetic surfaces resulting in a new structure called a magnetic island. Since islands make a path for heat and particles to move rapidly across it without crossing the equilibrium magnetic field, tearing modes degrade the particle confinement and lower the stored energy which in turn flattens the temperature (pressure) and density profiles inside the island. Large islands and the simultaneous existence of island chains even lead to a (major) disruption, with a fast loss of plasma energy (confinement) and a termination of the plasma.

The geometry of an island can be defined in terms of radial coordinate r, poloidal angle θ and introducing a new coordinate helical angle, ξ which is perpendicular to the equilibrium field lines at the $q = m/n$ surface,

$$\xi = \theta - \frac{n}{m}\phi, \tag{2.16}$$

and adopting large aspect ratio approximation, the equilibrium field along this direction is given by

$$B_h = B_\theta \left(1 - \frac{n}{m} q(r)\right), \tag{2.17}$$

where B_θ is the poloidal magnetic field. Close to the resonant rational surface, it becomes

$$B_h = -\left(B_\theta \frac{q'}{q}\right)_s (r - r_s). \tag{2.18}$$

In the Figure 2.2 the projection of a m/n island on $\xi - r$ plane can be seen where resonant radius, r_s denotes its minor radius. Magnetic islands can be interpreted as another set of helically nested flux surfaces with their own magnetic axis shown as O-point. Islands are bounded by the separatrices which are crossed at X-points in the poloidal cross section. The largest distance between the boundaries of magnetic island is given by w and called the full width of the island.

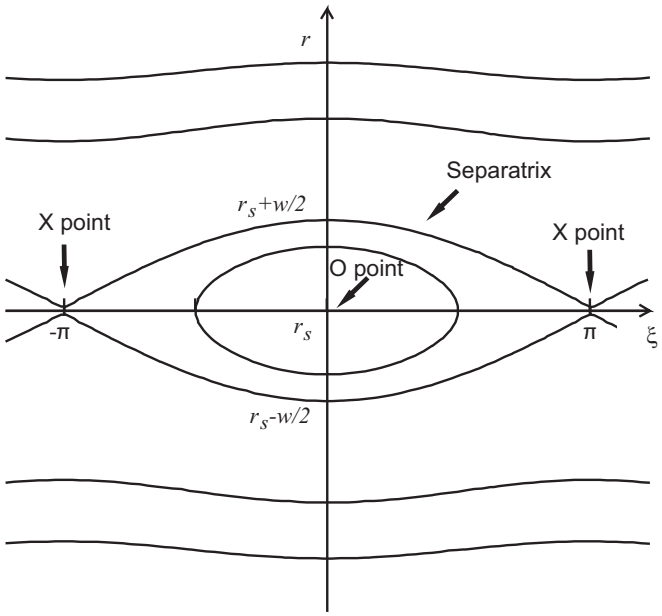

Figure 2.2: A schematic representation of a magnetic island [14].

Using field line equation

$$\frac{dr}{r_s d\xi} = \frac{B_r}{B_h} \tag{2.19}$$

The magnetic field perturbation in the radial direction can be written as

$$B_r = \widetilde{B_r}(r)\sin(m\xi) \tag{2.20}$$

assuming that $\widetilde{B_r}(r)$ remains constant over the radial extent of the island.

$$w = 4\sqrt{\frac{r_s \widetilde{B_r}(r_s) q(r_s)}{m B_\theta(r_s) q'(r_s)}} \tag{2.21}$$

It is practical to express the perturbed magnetic field in terms of the perturbed flux function, $\widetilde{\psi}$ [9] [19] [16]

$$\delta\vec{B} = \vec{\nabla}\phi \times \vec{\nabla}\widetilde{\psi}, \tag{2.22}$$

where

$$\widetilde{\psi} = \psi_1(r)\cos(m\theta - n\phi) = \psi_1(r)\cos(m\xi). \tag{2.23}$$

Assuming that ψ_1 is constant across the island region (known as constant ψ approximation),

$$\widetilde{B_r} = \frac{m\psi_1}{rR}. \tag{2.24}$$

Total magnetic field can also be expressed in terms of ψ_1 [19]

$$\vec{B} = RB_\phi\vec{\nabla}\phi + \vec{\nabla}\phi \times \vec{\nabla}\Upsilon \tag{2.25}$$

where the helical flux, Υ is composed of Ψ (poloidal magnetic flux) and $\widetilde{\psi}$

$$\Upsilon = \Psi + \widetilde{\psi} \tag{2.26}$$

It is convenient to define Ω which is the normalized flux surface label [5]

$$\Omega = \frac{\Upsilon}{\psi_1} = 8\frac{x^2}{w^2} - cos(m\xi) \tag{2.27}$$

where $x = r - r_s$ is the distance away from the rational surface. It varies between $\Omega = -1$ (at the O-point) and $\Omega = 1$ (at the separatrix) and $\Omega > 1$ defines flux surfaces outside the island.

2.5 Tearing modes

The relation between $\widetilde{\psi}$ and the current density perturbation parallel to the magnetic field, $J_{\|}$ can be found by Ampere's law. For an island whose width is much less than its resonant radius ($w<<r_s$), it reduces to [19]

$$\frac{1}{R}\,\Delta\widetilde{\psi} \simeq \frac{1}{R}\frac{\mathrm{d}^2\widetilde{\psi}}{\mathrm{d}r^2} = \mu_0 J_{\|}, \tag{2.28}$$

$$\frac{1}{R}\frac{\mathrm{d}^2\psi_1}{\mathrm{d}r^2}\cos(m\xi) = \mu_0 J_{\|}, \tag{2.29}$$

multiplying both sides by $\cos(m\xi)$,

$$\frac{1}{R}\frac{\mathrm{d}^2\psi_1}{\mathrm{d}r^2}\cos^2(m\xi) = \mu_0 J_{\|}\cos(m\xi), \tag{2.30}$$

since we are concerned with narrow islands, we integrate across the resonant surface from $r = r_s - \epsilon$ to $r = r_s + \epsilon$, where $\epsilon>>w$ is assumed. LHS becomes

$$\frac{r_s}{R}\int_{-\epsilon}^{\epsilon} dx \frac{\mathrm{d}^2\psi_1}{\mathrm{d}r^2}\oint d\xi\cos^2(m\xi) \tag{2.31}$$

$$= \frac{r_s}{R}\int_{-\epsilon}^{\epsilon} dx \frac{\mathrm{d}^2\psi_1}{\mathrm{d}r^2}\left|\frac{\xi}{2} + \frac{sin(2m\xi)}{4m}\right|_0^{2\pi} \tag{2.32}$$

$$= \frac{r_s\pi}{R}\left(\frac{\mathrm{d}\psi_1}{\mathrm{d}r}\right)_{r_s-\epsilon}^{r_s+\epsilon}. \tag{2.33}$$

Introducing classical stability index, Δ' which is defined as logarithmic jump of the radial derivative of the exterior solution for the perturbed magnetic flux function $\widetilde{\psi}$ across the rational surface,

$$\Delta' = \lim_{\epsilon\to 0}\frac{1}{\psi_1}\left[\frac{\mathrm{d}\psi_1}{\mathrm{d}r}\Big|_{r_s+\epsilon} - \frac{\mathrm{d}\psi_1}{\mathrm{d}r}\Big|_{r_s-\epsilon}\right], \tag{2.34}$$

the matching of the exterior solution to the interior one is obtained as,

$$\frac{1}{2}\Delta'\psi_1 = \mu_0 R\int_{-\epsilon}^{\epsilon} dx \oint \frac{d\xi}{2\pi}\cos(m\xi)J_{\|}. \tag{2.35}$$

Remembering that,

$$w = 4\sqrt{\frac{q\psi_1}{q'\psi'}}, \tag{2.36}$$

where $\psi' = \frac{\partial \psi}{\partial r}$ and $q' = \frac{\mathrm{d}q}{\mathrm{d}r}$, one can write,

$$\psi_1 = \frac{w^2 R B_p}{16 L_q}, \tag{2.37}$$

where $L_q = q/(dq/dr)$ is the magnetic shear length and positive for conventional tokamaks [8]. Substituting equation 2.37 into equation 2.35 and rearranging the terms, the form of equation is obtained which will be used in the coming sections to evaluate the effect of other terms resulting in stabilization or destabilization of magnetic islands

$$r_s \Delta' = \frac{16 \mu_0 L_q r_s}{B_p \pi w^2} \int_{-\epsilon}^{\epsilon} dx \oint d\xi \cos(m\xi) J_{\parallel}. \tag{2.38}$$

For the following calculations using flux surface averaging operator, $\bar{F}$ would ease our work. It is defined as $\bar{F} = \langle F \rangle \,/\, \langle 1 \rangle$, where

$$\langle F(\sigma, \Omega, \xi) \rangle \equiv \oint \frac{d\xi}{2\pi} \frac{F(\sigma, \Omega, \xi)}{\sqrt{\Omega + cos(m\xi)}}, \tag{2.39}$$

for $\Omega > 1$, and

$$\langle F(\sigma, \Omega, \xi) \rangle \equiv \int_{-\xi}^{\xi} \frac{d\xi}{2\pi} \frac{1/2[F(\sigma, \Omega, \xi) + F(-\sigma, \Omega, \xi)}{\sqrt{\Omega + cos(m\xi)}}, \tag{2.40}$$

for $-1 < \Omega < 1$. Here $\sigma = sgn(x)$, $\xi = cos^{-1}(-\Omega)/m$ and F is a general function with the property $\vec{B} \cdot \vec{\nabla} \langle F \rangle = 0$ [9] [5].

We continue keeping in mind that in the model being employed $\oint \frac{d\xi}{2\pi} = 2 \int_{-\xi}^{\xi} \frac{d\xi}{2\pi}$, so it can be written as the following,

$$\Delta' \psi_1 = 4 \mu_0 R \int_{-1}^{\infty} d\Omega \int_{-\xi}^{\xi} \frac{d\xi}{2\pi} \frac{w}{4\sqrt{2}} \frac{\cos(m\xi) J_{\parallel}}{\sqrt{\Omega + cos(m\xi)}}. \tag{2.41}$$

As can be seen, in order to continue the perturbed current parallel to the magnetic field should be determined. There are several contributions to the perturbed current but now we simply consider the induced current which

results from the island growth itself. Since $\tilde{E} = (1/R)(d\tilde{\psi}/dt)$, the perturbed current is related to the evolution of the poloidal flux perturbation through Ohm's law,

$$E = \eta(J - J_{CD}) - \tilde{\eta}J_0, \tag{2.42}$$

where J_{CD} is a part of the perturbed current that is driven non-inductively and $\tilde{\eta}J_0$ is a part of the current perturbation generated by a perturbation in the plasma resistivity. Neglecting for now these latter two contributions, the flux surface averaged parallel current can be written as [9] [19],

$$J_{\parallel} = \frac{\overline{E_{\parallel}}}{\eta} = \frac{1}{R\eta}\overline{\cos(m\xi)}\frac{\mathrm{d}\psi_1}{\mathrm{d}t}. \tag{2.43}$$

Substituting it into the equation 2.41 and employing the flux surface averaging operator, it reduces to

$$\Delta'\psi_1 = 4\mu_0 R\frac{1}{R\eta}\frac{\mathrm{d}\psi_1}{\mathrm{d}t}\int_{-1}^{\infty} d\Omega\frac{w}{4\sqrt{2}}\frac{\langle\cos(m\xi)\rangle^2}{\langle 1\rangle}. \tag{2.44}$$

Using the result of the integration which was given in [5],

$$\sqrt{2}\int_{-1}^{\infty} d\Omega\frac{\langle cos(m\xi)\rangle^2}{1} = 0.8227, \tag{2.45}$$

right hand side can be written as

$$\Delta' = 0.82\frac{\tau_r}{r_s^2}\frac{\mathrm{d}\psi_1/\mathrm{d}t}{\psi_1}\frac{w}{2}, \tag{2.46}$$

where $\tau_r = \frac{\mu_0 r_s^2}{\eta}$ is the current diffusion time. The ratio $\frac{\mathrm{d}\psi_1/\mathrm{d}t}{\psi_1}$ can be written in terms of the magnetic island width w

$$\frac{\mathrm{d}\psi_1/\mathrm{d}t}{\psi_1} = \frac{\mathrm{d}w}{\mathrm{d}t}\frac{2}{w}. \tag{2.47}$$

Putting it into the equation 2.47, we finally obtain the Rutherford equation (which is also called classical tearing mode equation) [13] [5] [19],

$$0.82\frac{\tau_r}{r_s}\frac{\mathrm{d}w}{\mathrm{d}t} = r_s\Delta'. \tag{2.48}$$

The Rutherford equation describes the growth or decay of a magnetic island of full width w. Δ' represents the free energy available in the plasma current density distribution to drive a tearing mode [19]. For small islands ($w<<r_s$), Δ' is not affected by the island itself so it is independent of w and when Δ' is positive, island grows linearly. As islands become sufficiently large, they will have an influence on the current profile around them so Δ' is no longer independent of w. Instead the dependence of Δ' on w can be expressed by the following approximation [3],

$$\Delta'(w) = \Delta'_0 \left(1 - \frac{w}{w_{sat}}\right), \tag{2.49}$$

where w_{sat} is the saturated island width. For $\Delta'>0$, an island grows to $w=w_{sat}$ till it consumes all its free energy leaving $\Delta'=0$.

2.6 Generalized Rutherford equation

Rutherford equation is derived under the assumption that the induced current resulting from the island growth is the only source of current perturbation parallel to the magnetic field. However, there are extra inductive or non-inductive helical current perturbations around the resonant surface modifying the classical tearing mode equation. With the introduction of these perturbations the modified equation is called the generalized Rutherford equation. It describes the temporal evolution of the full width w of a magnetic island as a function of different driving and stabilizing mechanisms [10]:

$$0.82\frac{\tau_r}{r_s}\frac{dw}{dt} = r_s\Delta' + \frac{16\mu_0 L_q r_s}{B_p \pi w^2}\int_{-\infty}^{\infty} dx \oint d\xi \left(\delta j_{\parallel,1} + \delta j_{\parallel,2} + ...\right) cos(m\xi), \tag{2.50}$$

where $\delta j_{\parallel}$ refers to the current perturbation given in Ohm's law. Subsequently, the contributions of other current perturbations are discussed in

the same order as given by the following equation,

$$0.82\frac{\tau_r}{r_s}\frac{dw}{dt} = r_s\Delta' + r_s\Delta'_{bs} + r_s\Delta'_{DED} - r_s\Delta'_{CD} - r_s\Delta'_H. \tag{2.51}$$

2.6.1 Neoclassical tearing modes

Neoclassical tearing modes (NTMs) are magnetic islands destabilized by the perturbation of the bootstrap current. Bootstrap current is a non-inductive current which is driven by the radial gradient of plasma pressure. It flows parallel to the magnetic field and is independent of the current driven by an applied electric field. It can be approximately written as [8]:

$$J_{bs} \approx -\left(\frac{\epsilon^{1/2}}{B_\theta}\right)\frac{\mathrm{d}p}{\mathrm{d}r}, \tag{2.52}$$

where $\epsilon = \frac{r}{R_0}$ is the local inverse aspect ratio for minor radius r and major radius R_0 and p is the plasma pressure.

As an initial (seed) magnetic island forms, pressure is flattened within the island separatrix resulting in a removal of the bootstrap current inside the island while there still exists bootstrap current outside. This helical perturbation of bootstrap current provides a destabilizing effect for conventional tokamaks (where magnetic shear length $L_q = q/\left(\mathrm{d}q/\mathrm{d}r\right)$ is positive and pressure gradient is negative) to reinforce the initial island.

The resulting equation expressing the temporal evolution of full width w of an island including neoclassical effects is called modified Rutherford equation [8] [19] [17],

$$0.82\frac{\tau_r}{r_s}\frac{dw}{dt} = r_s\Delta' - c_{neo}\beta_p\varepsilon^{1/2}\frac{L_q}{L_p}\frac{r_s}{w}, \tag{2.53}$$

where $\beta_p = \frac{2\mu_0 p}{B_\theta^2}$ is the poloidal beta, $L_p = p/\left(\mathrm{d}p/\mathrm{d}r\right)$ is the pressure gradient length and c_{neo} is a constant of order one. Classically stable plasmas ($\Delta' < 0$) can be destabilized by the helically perturbed bootstrap current

which is called the neoclassical tearing modes (NTMs) [19]. Under this condition equation 2.53 implies that every island on a rational surface would be destabilized although this is indeed not the case. Fortunately, so-called small island effects form threshold mechanisms and prevent NTMs to become totally unstable and harmful to the confinement.

First of those effects result from the fact that at small island widths, temperature and density are not necessarily flux functions (consequently, pressure is also not a flux function). Consequently, the flattening of pressure inside such an island would not be complete which would put a threshold on the occurrence of NTMs. Including this effect, modified Rutherford equation can be written as [17] [8]:

$$0.82\frac{\tau_r}{r_s}\frac{dw}{dt} = r_s\Delta' - c_{neo}\beta_p\epsilon^{1/2}\frac{L_q}{L_p}\frac{r_s}{w}\frac{w^2}{w^2+w_c^2}, \tag{2.54}$$

where w_c is the critical island width below which the pressure is not flattened within the island separatrix. It is proportional to the ratio of thermal diffusivities parallel and perpendicular to the magnetic field and $w_c \approx 1$ cm under typical tokamak conditions [19] [8].

A second small island effect is the polarization current which is mostly stabilizing. As the islands rotate at a frequency ω in the frame of the plasma flow, a time varying electric field forms. Since the response of electrons to this electric field is faster than that of the ions, another current which is called polarization current is generated. Its characteristic threshold island width is $w_{pol} \approx (L_q/L_p)^{1/2}\epsilon^{1/2}\rho_{\theta i}$ where $\rho_{\theta i}$ is ion banana width. With the inclusion of this final threshold mechanism, contribution of perturbed bootstrap current can be written as,

$$r_s\Delta'_{bs} \approx -\epsilon^{1/2}\frac{L_q}{L_p}\beta_p\frac{r_s}{w}\left[\frac{w^2}{w^2+w_c^2} - \frac{w_{pol}^2}{w^2}\right] \tag{2.55}$$

2.6.2 Dynamic ergodic divertor (DED)

Magnetic islands can also be excited by externally resonant magnetic perturbation fields. On TEXTOR tokamak, these perturbed fields are generated by the dynamic ergodic divertor (DED) [3]. DED consists of a set of helical perturbation coils located at the high field side of the tokamak. Current application to these helical coils leads to a magnetic perturbation. In the absence of a conducting plasma, the vacuum magnetic field (the superposition of the DED perturbation field and the equilibrium magnetic field) results in a 'fictive' island called vacuum island. In the presence of a conducting plasma, this perturbation field generates shielding currents on rational q surfaces and these currents influence the stability of tearing modes. In this case, the vacuum island only represents the amplitude and phase of the perturbation field.

The contribution of destabilization by DED to the Rutherford equation is given by:

$$r_s \Delta'_{DED} = 2m \left(\frac{w_{vac}}{w} \right)^2 \cos\left(\Delta\left(m\xi \right) \right), \tag{2.56}$$

where

$$\Delta\left(m\xi \right) = m\left(\xi_{O,plasma} - \xi_{O,vacuum} \right) \tag{2.57}$$

is the phase difference between the O-points of the plasma and the vacuum island and w_{vac} is the width of the latter. The islands driven by DED discussed in this research [3] [17] are locked to the perturbation field of DED, ($\Delta\xi = 0$) and have vacuum islands of about 4 cm wide. It has been observed in [3] that after switching off the DED, the 2/1 magnetic island still remains without considerable changes in its width.

2.6.3 Current drive

Perturbed current profile can be compensated through a non-inductive current. It can be driven by ECW deposition inside the island. A co-current drive can stabilize the magnetic island on the contrary a counter-current drive provides extra perturbed current profile and results in a destabilization of the magnetic island. A normalized Gaussian distribution is assumed for the radial power deposition profile,

$$P_{EC} = P_{tot}\tilde{P}_{CW}(x)\mathcal{M}(\xi;\mathcal{D},\phi), \tag{2.58}$$

with

$$\tilde{P}_{CW}(x) = \frac{1}{2\pi^{5/2}w_{dep}Rr_s}e^{-4(x-x_{dep})^2/w_{dep}^2} \tag{2.59}$$

where w_{dep} is the full e^{-1} power density width and $x_{dep} = r_{dep} - r_s$ is the deposition dislocation relative to the resonant radius. The total injected power in case of continuous wave (CW) application is represented by P_{tot} and the modulation effects are included in the function $\mathcal{M}$ which is written in terms of a Heaviside function as

$$\mathcal{M}(\xi;\mathcal{D},\phi) = H\left(\left|\cos\left(m\xi/2+2\right) - \cos\left(\mathcal{D}\pi/2\right)\right|\right), \tag{2.60}$$

where ξ is the helical angle, $\mathcal{D}$ the power on-time fraction, and ϕ the phase mismatch between the power modulation and the island rotation. The relation between the non-inductive current driven by EC power absorption and power density averaged over a flux surface is given by:

$$\overline{J_{CD}} = 2\pi R\eta_{CD}\overline{P_{EC}} \tag{2.61}$$

where current drive efficiency η_{CD} is defined as

$$\eta_{CD} = \frac{I_{CD}}{P_{tot}}, \tag{2.62}$$

and assumed to be constant over the deposition profile. Making use of equation 2.86, one can find the contribution of current drive to the generalized Rutherford equation,

$$r_s\Delta'_{CD} = \frac{16\mu_0 L_q r_s}{B_p \pi w^2} \int_{-\infty}^{\infty} dx \oint d\xi \overline{J_{CD}} cos(m\xi), \tag{2.63}$$

which is equal to

$$r_s\Delta'_{CD} = \frac{16\mu_0 L_q r_s}{B_p \pi w^2} \int_{-1}^{\infty} d\Omega \overline{P_{EC}} 2\pi R \eta_{CD} \oint d\xi \frac{cos(m\xi)}{\sqrt{\Omega + cos(m\xi)}} \frac{w}{4\sqrt{2}}. \tag{2.64}$$

As given in [10] which was found following the formulation of [15], the term $r_s\Delta'_{CD}$ is written as,

$$r_s\Delta'_{CD} \approx \frac{16\mu_0 L_q}{B_p \pi} \frac{\eta_{CD} P_{tot}}{w_{dep}^2} F_{CD}(w^\star, x_{dep}, \mathcal{D}). \tag{2.65}$$

Note that its contribution has been defined in terms of an efficiency forefactor times a dimensionless effectivity, F_{CD}. Geometrical parameters like the normalized island width ($w^* = w/w_{dep}$), the displacement of the power deposition from the resonant surface and the modulation are embedded in the function F_{CD} given by,

$$F_{CD}(w^\star, x_{dep}, \mathcal{D}) = \frac{w_{dep}^2 \int_{-1}^{\infty} d\Omega \overline{\tilde{p}_{CW} \mathcal{M}} \langle cos(m\xi) \rangle}{w^2 \int_{-1}^{\infty} d\Omega \overline{\tilde{p}_{CW}} \langle 1 \rangle}. \tag{2.66}$$

2.6.4 Local heating

The ECW deposition inside the island can stabilize the mode not only directly through a non-inductive current but also indirectly, by a perturbation of the temperature profile resulting in a perturbation of the inductive current J_H. This current perturbation can be approximated making use of the resistivity relation given by the equation 2.8 as,

$$J_H \approx \frac{J_{sep}}{T_{sep}^{3/2}} \delta \left(T_e^{3/2} \right) \tag{2.67}$$

where J_{sep} and T_{sep} denote the inductive part of the current density and the temperature at the island separatrix, respectively.

As can be seen from the equation above, in order to evaluate current perturbation, it is necessary to solve heat diffusion equation below so that δT_e can be found. Keeping in mind the time scales of interest, we assume that T_e equilibrates along the perturbed field lines, so that $T_e = T_e(\Omega)$.

$$\frac{\partial T_e}{\partial t} + \overline{div\vec{g}} = \frac{\partial T_e}{\partial t} + \frac{\partial \Gamma}{\partial V} = \overline{P_{EC}}(\Omega) \tag{2.68}$$

where $\vec{g}$ is the local flux, and Γ is the net flux of the vector $\vec{g}$ through the whole magnetic surface,

$$\vec{g}(\Omega,\theta) = T_e(\Omega)\vec{\nu}(\Omega,\theta) - D(\Omega,\theta)\vec{\nabla}T_e(\Omega), \tag{2.69}$$

$$\Gamma = \int div\vec{g}dV = \overline{\vec{g}\cdot\vec{\nabla}V}, \tag{2.70}$$

with $D = n_e\chi_\perp k_B$, and n_e is the electron density, $\chi_\perp$ is the perpendicular heat conductivity which is assumed to be constant, k_B is the Boltzmann constant (in units of J/keV).

Under steady state conditions(for $\tau_r >> \tau_{diff}$ with $\tau_{diff} = w^2/\chi_\perp$) and neglecting convection in the heat diffusion equation, we get

$$\overline{P_{EC}} = -\frac{\partial\Omega}{\partial V}\frac{\partial}{\partial\Omega}\left(\frac{\partial V}{\partial\Omega}\overline{\left|\vec{\nabla}\Omega\right|}n_e\chi_\perp k_B\frac{\partial T_e}{\partial\Omega}\right), \tag{2.71}$$

where $V(\Omega)$ is the total volume enclosed within a given flux surface,

$$V = 2\pi R\int r_s dx\oint d\xi, \tag{2.72}$$

and accordingly, $\frac{\partial V}{\partial\Omega}$ is the volume of the flux shell which can be shown to be equal to

$$\frac{\partial V}{\partial\Omega} = 8\pi^2 R r_s\frac{w}{4\sqrt{2}}\left\langle 1\right\rangle. \tag{2.73}$$

Substituting it in the previous equation, we obtain

$$\overline{P_{EC}}\partial V = -\partial\left(8\pi^2 R r_s\frac{w}{4\sqrt{2}} < |\vec{\nabla}\Omega|^2 > n_e\chi_\perp k_B\frac{\partial T_e}{\partial\Omega}\right). \tag{2.74}$$

Integrating both sides over Ω once gives us,

$$P(\Omega) = - < |\vec{\nabla}\Omega|^2 > n_e \chi_\perp k_B \frac{\partial T_e}{\partial \Omega} \tag{2.75}$$

$P(\Omega)$ is the total power injected inside the flux tube between the O-point and the flux surface labeled Ω. Integrating once more over Ω an expression for temperature perturbation is found as,

$$T_e = T_{sep} + \delta T_e, \tag{2.76}$$

$$\delta T_e = \frac{P_{tot} w}{8\pi^2 R r_s n_e \chi_\perp k_B} \delta \tilde{T}_e, \tag{2.77}$$

where

$$\delta \tilde{T}_e = \int_\Omega^1 d\Omega \frac{\tilde{P}(\Omega)}{< |\vec{\nabla}\Omega|^2 >} \frac{8\pi^2 R r_s}{w}, \tag{2.78}$$

and

$$P(\Omega) = P_{tot} \tilde{P}(\Omega). \tag{2.79}$$

$\delta \tilde{T}_e$ is dimensionless and called normalized temperature perturbation. The current perturbation $J_H \propto \delta \left(T_e^{3/2} \right)$ can be further reduced by the following approximation,

$$\delta(T_e^{3/2}) = (T_{sep} + \delta T_e)^{3/2} - T_{sep}^{3/2} \approx T_{sep}^{1/2} \frac{3}{2} \delta T_e \tag{2.80}$$

$$J_H \approx \frac{J_{sep}}{T_{sep}} \frac{3}{2} \delta T_e \tag{2.81}$$

The stabilization term provided by local heating is to be calculated from the following equation

$$r_s \Delta'_H = \frac{16 \mu_0 L_q r_s}{B_p \pi w^2} \int_{-w/2}^{w/2} dx \oint d\xi J_H cos(m\xi), \tag{2.82}$$

which is equal to

$$r_s \Delta'_H = \frac{16 \mu_0 L_q r_s}{B_p \pi w^2} \int_{-1}^{1} d\Omega J_H \oint d\xi \frac{cos(m\xi)}{\sqrt{\Omega + cos(m\xi)}} \frac{w}{4\sqrt{2}}. \tag{2.83}$$

Substituting the approximated J_H into the equation above, a new expression for stabilization term $(r_s\Delta'_H)$ is obtained [10]:

$$r_s\Delta'_H \approx \frac{16\mu_0 L_q}{B_p\pi}\frac{\eta_H P_{tot}}{w_{dep}^2}F_H(w^\star, x_{dep}, \mathcal{D}) \tag{2.84}$$

where η_H denotes the efficiency with which the power is converted into a perturbative inductive current and the geometrical parameters are embedded in the dimensionless function F_H,

$$\eta_H = \frac{3w_{dep}^2}{8\pi R n_e \chi_\perp k_B}\frac{J_{sep}}{T_{sep}}, \tag{2.85}$$

$$F_H(w^\star, x_{dep}, \mathcal{D}) = \frac{1}{2\pi w}\int_{-1}^{1} d\Omega\delta\tilde{T}_e \oint d\xi \frac{w}{4\sqrt{2}}\frac{cos(m\xi)}{\sqrt{\Omega + cos(m\xi)}}. \tag{2.86}$$

The temperature profile above has been obtained under the assumption of a constant heat conductivity. In order to investigate the possible consequences of constant $\chi_\perp$ profiles, a family of possible T_e profiles is introduced, characterized by the single parameter α as

$$T_e(\Omega;\alpha) = (T_{O-point} - T_{sep})\left(1 - \left((\Omega+1)/2\right)^\alpha\right) + T_{sep}, \tag{2.87}$$

where $T_{O-point}$ is the temperature at $\Omega = -1$ and T_{sep} is the temperature at $\Omega = 1$.

Note that in this profile the values of $T_{O-point}$ and T_{sep} are independent of the parameter, α. According to this new temperature profile, temperature perturbation inside the island is given by

$$\delta T_e(\Omega;\alpha) = (T_{O-point} - T_{sep})\left(1 - \left((\Omega+1)/2\right)^\alpha\right). \tag{2.88}$$

By changing α, a family of temperature perturbation profiles can be obtained. It is necessary to know if the temperature profile which was obtained in the preceding section to be used for evaluating the ECRH stabilizing term

in this research is within the range of this new temperature profile (to avoid confusion, it will be represented as T_α). To see this, the normalized temperature perturbation, $\delta\tilde{T}_e$ of both profiles should be compared qualitatively. In order to keep the calculations simple, let us assume the power deposition to be aligned on resonant surface, r_s ($x_{dep} = 0$), continuous ($D = 1$). This comparison has been restricted to three different normalized island width, ($w^* = w/w_{dep}$), $w^* = 0.3$, $w^* = 1$ and $w^* = 3$. Respectively, they represent the cases when island width is smaller than deposition width of power, when they are equal, and when island width is larger than the deposition width.

Figures 2.3 - 2.5 show the comparison of normalized temperature perturbation profiles inside the island for the case of $w^* = 0.3$, $w^* = 1$ and $w^* = 3$, respectively. For each comparison above the values of the parameter, α have been kept the same. One of conclusions is that T_e profile (the one adopted for calculating ECRH term for the rest of this research) stays always within the range of T_α profiles i.e. in the family of T_α profiles for each different w^* case. Moreover, it can be observed that α_{fit} values are 1, approximately 1 and around 0.8 for normalized island width $w^* = 0.3$, $w^* = 1$ and $w^* = 3$, respectively. This indicates that α_{fit} value slightly decreases as w^* increases.

When the difference between $\delta\tilde{T}_{O-point}$ and $\delta\tilde{T}_{sep}$ is considered for each graph, another conclusion can be drawn. For a given power deposition width,w_{dep} as the island width decreases, the difference in perturbation also decreases. The difference between $T_{O-point}$ and T_{sep} is the highest for $w^* = 3$ case among all these three cases. Power deposition whose density width is smaller than island width results in a more efficient temperature perturbation.

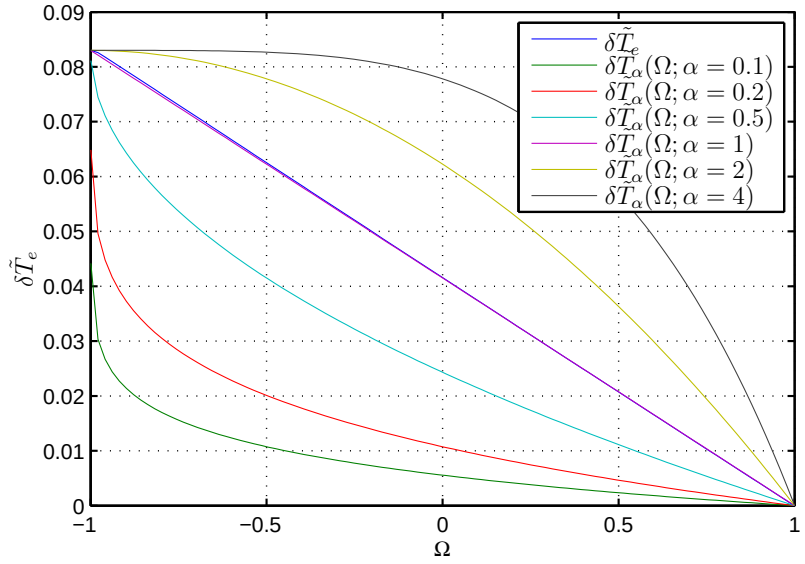

Figure 2.3:
Comparison of normalized temperature perturbation profiles for $w^* = 0.3$ resulting from CW power deposition without misalignment

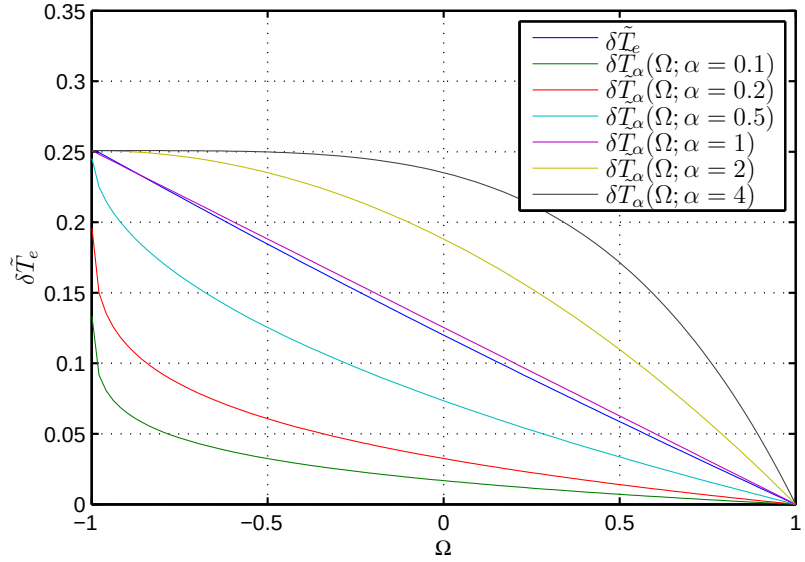

Figure 2.4:
Comparison of normalized temperature perturbation profiles for $w^* = 1$ resulting from CW power deposition without misalignment

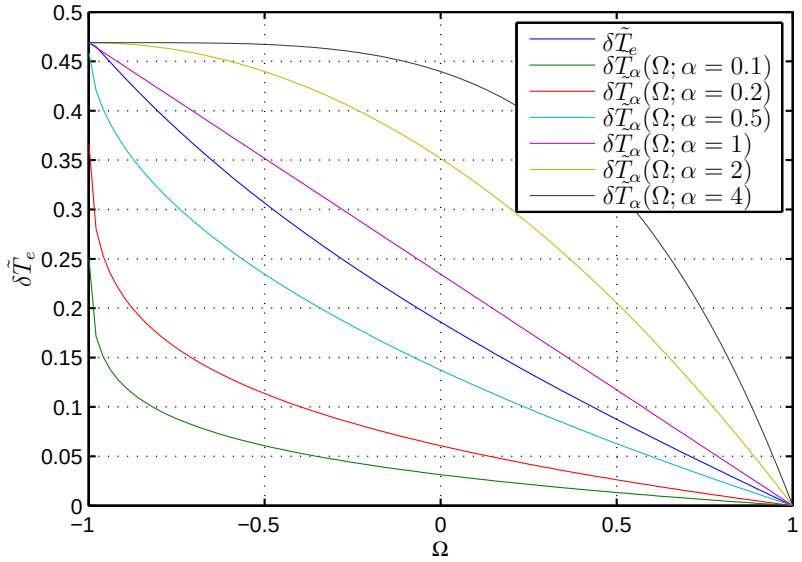

Figure 2.5:
Comparison of normalized temperature perturbation profiles for $w^* = 3$ resulting from CW power deposition without misalignment

Another comparison can be made with respect to the F_H values of those profiles have at three different normalized island width, ($w^* = w/w_{dep}$), $w^* = 0.3$, $w^* = 1$ and $w^* = 3$, under the same assumptions made for temperature profile comparison. In order to provide coherency, same values of α have been chosen as before. As can be seen from the Figure 2.6, the three values of F_H which were calculated using the temperature profile T_e, again stay within the range of their corresponding F_H values calculated from the temperature profile T_α.

These results confirm the fitted α value found in the previous comparison of normalized temperature perturbation profiles for each w^* case. Moreover, the F_H values of each profile follow the same trend i.e. as normalized island width increases, the corresponding values also increase (within the range

$0.3 \leq w^* \leq 3$). Detailed information about this trend can be found in [10], where it was obtained from numerical evaluation of equation 2.86, that F_H values are approximately linear for small values of w^* and converge to a constant for $w^* >> 1$.

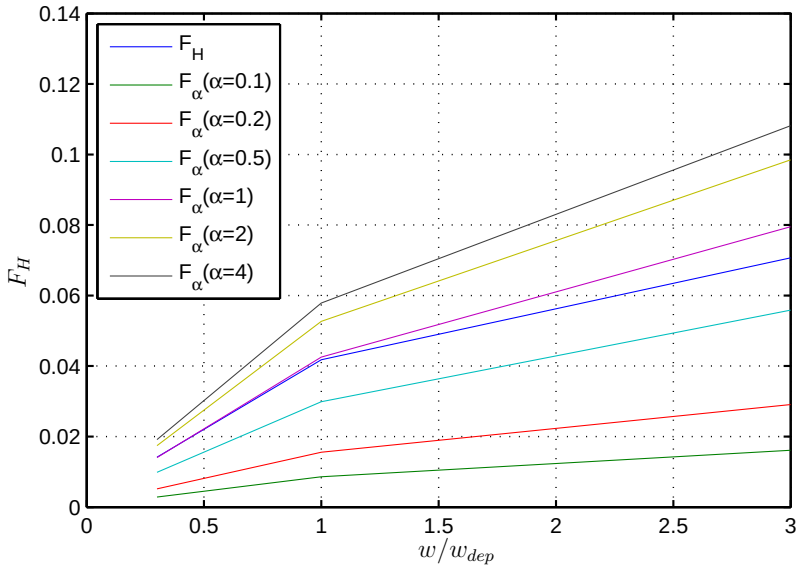

Figure 2.6:
Comparison of F_H values as a function of normalized island width of each profile being discussed

There is one more conclusion to be drawn on α dependence of F_H values. While broader T_α profiles lead to higher F_H values, lower F_H values are obtained from more peaked T_α profiles.

CHAPTER 3

COMPARISON WITH EXPERIMENTAL $T_e(\Omega)$ PROFILES

In this chapter we shall start with working on the measured temperature profiles inside the suppressed magnetic islands [3]. The fact that in the theoretical model perpendicular heat conductivity, $\chi_\perp$ is assumed to be constant leads us to find out its value for each experimental case that will be discussed in this chapter. In the first section the method used for obtaining $\chi_\perp$ inside the island is discussed and the values are found out. In the second section by considering the experimental conditions (basically the input powers) and the results, the choice of $\chi_\perp$ is fixed to be used for the rest of the research.

3.1 How to obtain $\chi_\perp$

Let us start with rewriting the expression of temperature profile calculated in the preceding chapter,

$$T_e(\Omega) = T_{sep} + \delta T_e\left(\Omega\right), \tag{3.1}$$

where

$$\delta T_e = \frac{P_{tot} w}{8\pi^2 R r_s \chi_\perp n_e k_B} \delta\tilde{T}_e, \tag{3.2}$$

and

$$\delta\tilde{T}_e = \int_\Omega^1 d\Omega \frac{\tilde{P}|_{-1}^{\Omega}}{< |\vec{\nabla}\Omega|^2 >} \frac{8\pi^2 R r_s}{w}. \tag{3.3}$$

It should be reminded that this temperature profile was calculated under the assumption $\chi_\perp$ is constant. $\delta\tilde{T}_e$ is, by definition, independent of P_{tot} and $\chi_\perp$. This fact is the starting point to obtain $\chi_\perp$ value inside the island using experimental data.

Before proceeding further, let us explain the experiment which was conducted on the TEXTOR tokamak briefly. Owing to the Dynamic Ergodic Divertor (DED) that TEXTOR has, islands can be created and controlled with a fully known driving term [3]. When the DED current exceeds a threshold, islands can be destabilized. In this experiment only a 2/1 island was destabilized which after a while, has reached a saturated island width of about 12 cm. Then ERCH was switched on, depositing CW power of 400 kW, 300 kW, 200 kW, on the resonant $q = 2$ surface reducing the width of the island respectively to 5 cm, 6 cm, 7 cm.

For each case, there are two ways to calculate $\delta\tilde{T}_e(\Omega = -1)$. First way comes from numerical calculation of equation 3.3. In the numerical calculation the conditions of the experiments are mimicked ($x_{dep} = 0$, $\mathcal{D} = 1$, and $\phi = 0$). The $\delta\tilde{T}_{sim}(\Omega = -1)$ curve under these conditions as a function of w/w_{dep}, ($w_{dep} = 1.8$ cm) is shown in Figure 3.1.

The second way comes from the experimental calculation and is given by

$$\delta\tilde{T}_{exp}(\Omega = -1) = \left(\frac{P_{tot} w}{8\pi^2 R r_s \chi_\perp n_e k_B}\right)^{-1} (T_{O-point} - T_{sep}) \,, \tag{3.4}$$

where the difference between $T_{O-point}$ and T_{sep} is to be found from experimental data. It is shown in [3] that over the largest part of the island, $\chi_\perp$ is about 1 to 1.5 m^2/s. In Figure 3.1 the $\delta\tilde{T}_{exp}(\Omega = -1)$ values calculated assuming $\chi_\perp = 1.5$ m^2/s can be seen.

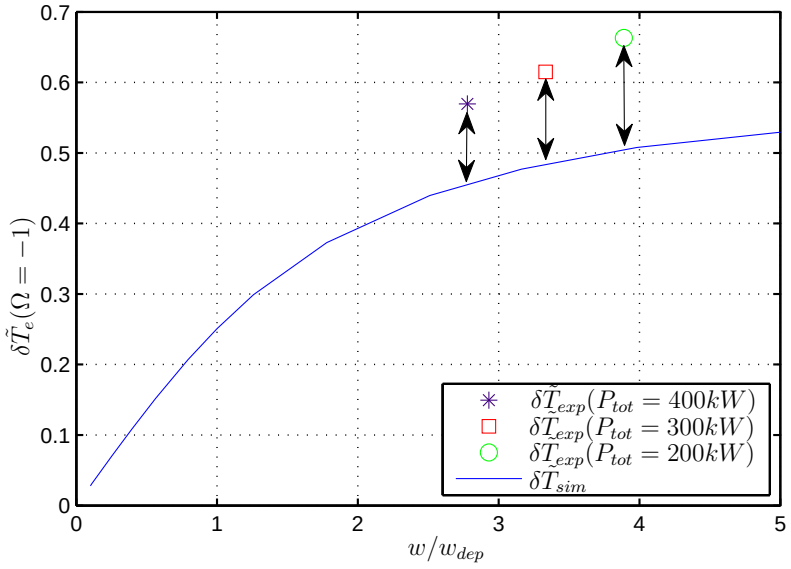

Figure 3.1:
$\delta\tilde{T}_e(\Omega = -1)$ values found from experimental data taking $\chi_\perp = 1.5$ m^2/s and its numerically calculated curve.

However, this choice of $\chi_\perp$ does not provide the same values as $\delta\tilde{T}_e(sim)$ does for these three cases. The question to be asked is what $\chi_\perp$ value should be chosen so that both ways give the same result. The $\chi_\perp$ can be found from the relation below,

$$\frac{\delta\tilde{T}_e(exp)}{1.5m^2/s}\chi_\perp = \delta\tilde{T}_e(sim), \tag{3.5}$$

which gives us the following values,

$$\chi_\perp(P_{tot} = 400\ kW) = 1.2032, \tag{3.6}$$

$$\chi_\perp(P_{tot} = 300\ kW) = 1.1819, \tag{3.7}$$

$$\chi_\perp(P_{tot} = 200\ kW) = 1.1419. \tag{3.8}$$

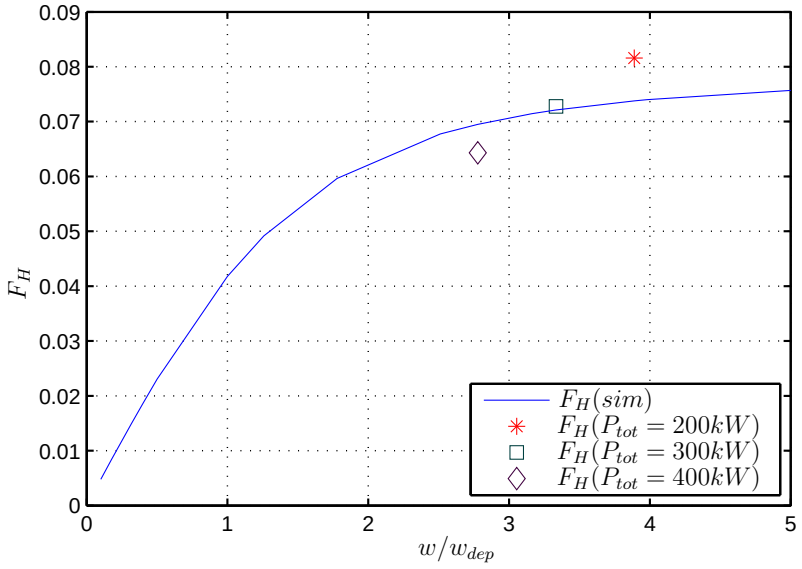

Figure 3.2:
F_H values found from simulation as a function of w/w_{dep} and F_H experimental values calculated using their associated $\chi_\perp$.

It is also necessary to check whether F_H(experimental) values calculated using their associated $\chi_\perp$ are the same as the ones calculated theoretically. Figure 3.2 shows that only for the case whose input power is 300 kW, the results are quite close. In order to see the reason of this difference in F_H values both theoretical and experimental $\delta\tilde{T}_e$ vs Ω curves have been plotted for each case (see Figure 3.3 - 3.5).

Figure 3.3 shows the theoretical and measured normalized temperature profiles inside the fully suppressed island $w_{supp} = 5$ cm after CW ECRH input power 400 kW. For this case that the area under the theoretical $\delta\tilde{T}_e$ curve is larger than one under the experimental curve can be accounted for the result that its experimental value of F_H is smaller than its theoretical value. Similarly, the quantitative difference in the area under the theoret-

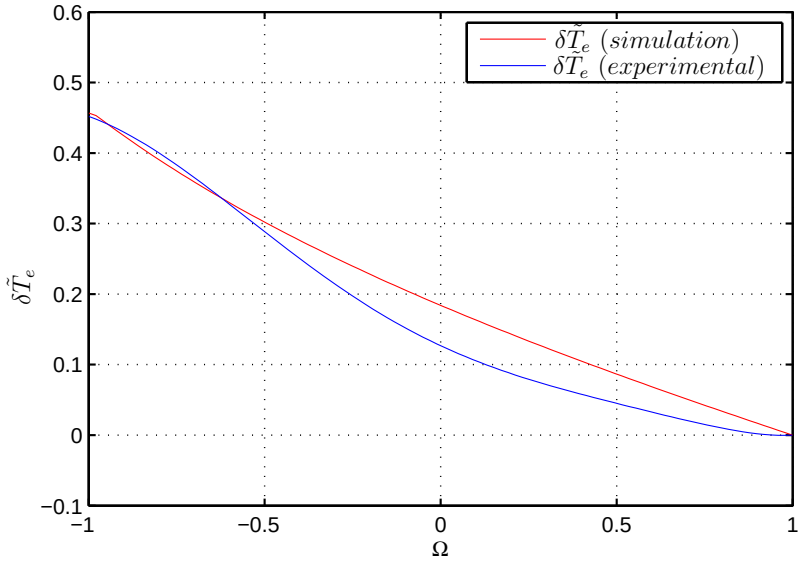

Figure 3.3:
Normalized temperature profiles inside the fully suppressed island after CW ECRH input power 400 kW, $w_{supp} = 5$ cm.

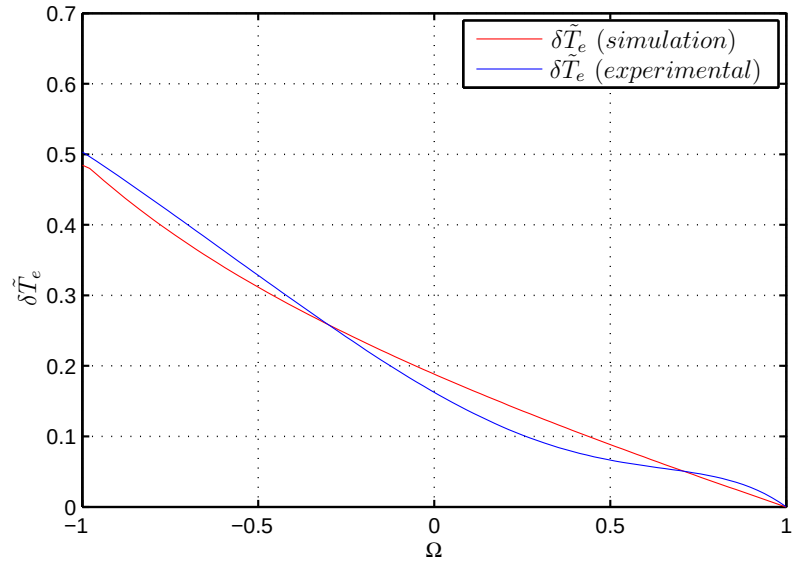

Figure 3.4:
Normalized temperature profiles inside the fully suppressed island after CW ECRH input power 300 kW, $w_{supp} = 6$ cm.

ical and measured curves of the other two cases reveals the difference in theoretical and experimental F_H values.

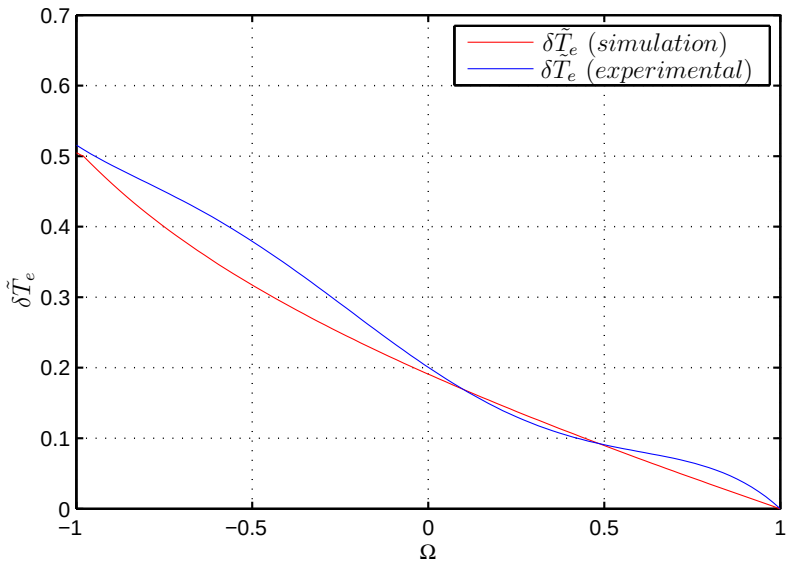

Figure 3.5:
Normalized temperature profiles inside the fully suppressed island after CW ECRH input power 200 kW, $w_{supp} = 7$ cm.

3.2 Fixing the choice of $\chi_\perp$

When the results are compared, it is obvious to see that different input powers do not result in considerable changes in the values of $\chi_\perp$. It is concluded that input power has no effect on $\chi_\perp$ and $\chi_\perp$ is not a function of ECRH power. For the rest of the research $\chi_\perp$ will be taken as 1.2 m^2/s regardless of the input power.

CHAPTER 4

GENERALIZED RUTHERFORD EQUATION SIMULATIONS

In ITER the control of neoclassical tearing modes (NTMs) is one of the main challenges in order to keep the plasma pressure stable and high and consequently to produce efficient energy. Electron cyclotron resonance heating (ECRH) and electron cyclotron current drive (ECCD) are the widely used two control methods although the effect of ECRH is often underestimated. Experiments were performed to see how effective ECRH can be on suppressing $m = 2, n = 1$ magnetic islands on TEXTOR tokamak. The controlled experiments can be divided into three groups. At first, the influence of variation in radial deposition of ECRH power on the suppression of magnetic islands is discussed. The second part aims to assess the effect that ECCD has on island suppression. Finally, modulated ECRH experiments were performed to observe under what conditions one can have the best outcome of ECRH mechanism. The results [17] have shown that in TEXTOR island stabilization by ECRH has a dominance over stabilization by ECCD. After having fixed the choice of $\chi_\perp$ which is approximately 1.2 m^2/s (independent of the input power to be used for TEXTOR simulations), the results of the generalized Rutherford equation shall be compared with TEXTOR data presented in [17]. First of all, general information regarding these three sets of experiments is given.

4.1 General overview on experiments

Let us recall the generalized Rutherford equation,

$$0.82\frac{\tau_r}{r_s}\frac{dw}{dt} = r_s\Delta' + r_s\Delta'_{bs} + r_s\Delta'_{DED} - r_s\Delta'_{CD} - r_s\Delta'_H \tag{4.1}$$

which describes the evolution of full width (w) of a magnetic island in terms of stabilizing and driving mechanisms. Since the experiments were performed at low β_p, the contribution of Δ'_{bs} is insignificant and can be ignored. In this case dynamic ergodic divertor (DED) was used to produce magnetic islands. Generalized Rutherford equation reduces to the following form,

$$0.82\frac{\tau_r}{r_s}\frac{dw}{dt} = r_s\Delta'(w) + r_s\Delta'_{DED} - r_s\Delta'_{CD} - r_s\Delta'_H. \tag{4.2}$$

In Figure 4.1 one can see the time traces of one of the discharges (Shot Nr. 94727). In this discharge $m = 2, n = 1$ DED generated magnetic island was suppressed only by ECRH (140 GHz, 770 kW) on $q = 2$ surface ($r_s = 0.28$ m). The growth and suppression of the island can be observed from the oscillations taking place on the 141 GHz ECE channel which measures the radiation temperature on the high-field side coming from a region approximately 3 cm inside the $q = 2$ surface. Increase in the oscillations results from DED operation and shows that 2/1 island is growing while suppression of the oscillations, as ECRH is switched on, implies island stabilization.

Experimental data were found out under the assumption that ΔT is proportional to the width of the island. That is why, experimental ratio of saturated island width before ECRH is switched on (basically, represented as w_{DED}) over the suppressed island width as a result of ECRH (represented as w_{ECRH}) is approximated as,

$$w_{DED}/w_{ECRH} = \Delta T_{ECRH}[\%]/\Delta T_{DED}[\%]. \tag{4.3}$$

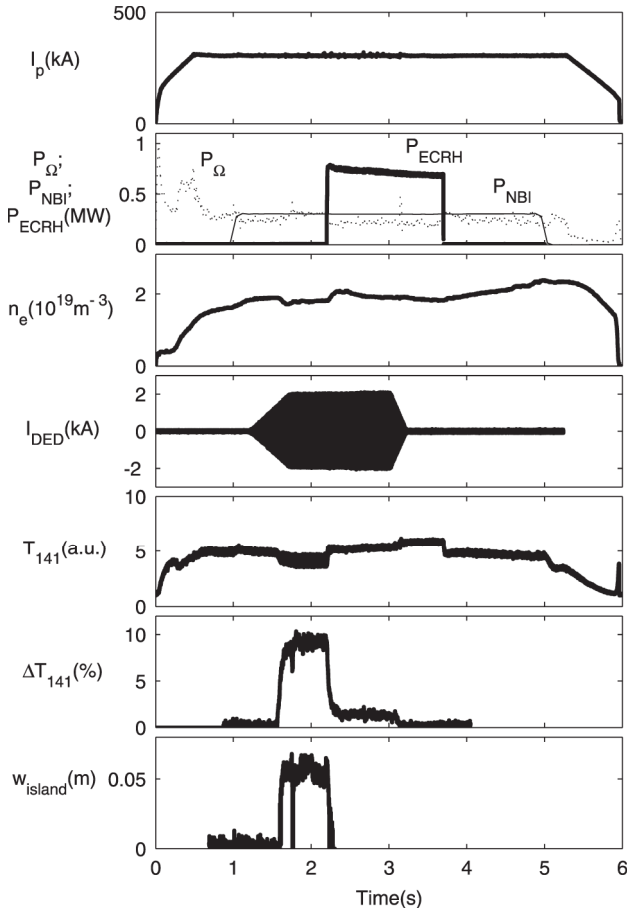

Figure 4.1:
Time traces of discharge 94727 in which a 2/1 magnetic island is created by DED and almost completely suppressed by ECRH at the $q = 2$ surface:(a) the plasma current; (b) plasma heating powers P_Ω, P_{NBI}, P_{ECRH}; (c) the line average density at $R = 1.80$; (d) the current in a DED coil; (e) the ECE radiation temperature at 141 GHz, T_{141}; (f) the amplitude of the 1 kHz oscillation in this signal, ΔT_{141}; (g) the island size measured by a soft x-ray camera [17].

Numerically calculated saturated island size is the island size $w = w_{sat}$ for which $\frac{dw}{dt} = 0$. The value of w_{DED} is evaluated from the generalized Rutherford equation in the following form,

$$0.82\frac{\tau_r}{r_s}\frac{dw}{dt} = r_s\Delta'(w) + r_s\Delta'_{DED}, \tag{4.4}$$

where $\Delta'(w) = \frac{-6.22w+0.627}{(0.23)^2}$ for TEXTOR experiments [3]. Another necessary parameter is the resonant radius $r_s = 0.28$ m. Note that the stabilizing ECRH and ECCD terms are dropped. For the calculation of w_{ECRH} all the terms are kept as in the equation 4.2. The islands driven by DED in these three sets of experiments are locked to the perturbation field of DED, ($\Delta\xi = 0$). In this case the contribution of DED term is written as,

$$r_s\Delta'_{DED} = 2m\left(\frac{w_{vac}}{w}\right)^2, \tag{4.5}$$

and the vacuum island width is chosen to be the same as in [3] which is of about 4 cm wide.

4.2 Comparison concerning radial deposition scans

In the first set of the experiments radial deposition variation of ECRH power of 750 kW was obtained by scanning the vertical injection angle for two different toroidal injection angles: $\phi = +0.5°$ and $\phi = -16°$ which correspond to the deposition width of $w_{dep} = 1.2$ cm and $w_{dep} = 4.6$ cm, respectively.

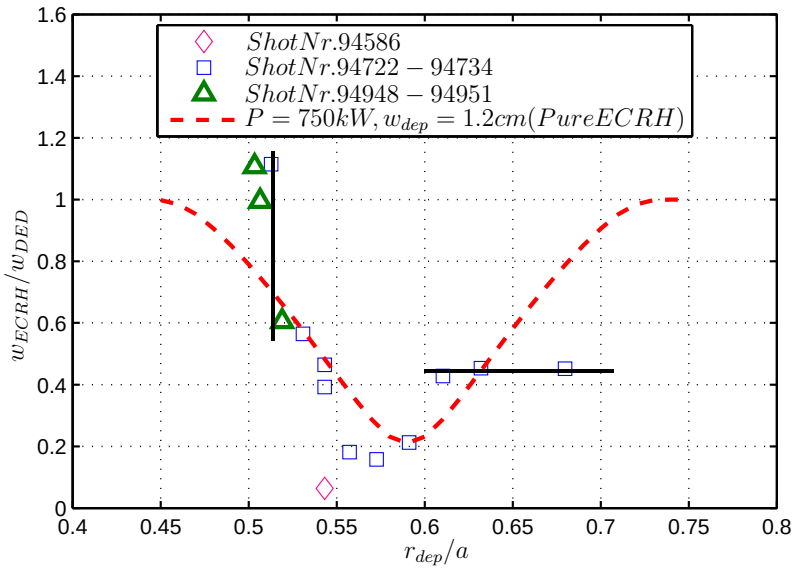

Figure 4.2:
Suppression of the 2/1 magnetic island as a function of radial deposition (where a= 47 cm is the minor radius of the tokamak) for narrow deposition profile($w_{dep} = 1.2$ cm). Red dashed curve shows the numerical results taking ECRH into account as the only stabilizing effect in the simulation. Different symbols refer to the data taken on different days, for which q= 2 surface position might have been slightly different.

For the case at narrow deposition profile ($w_{dep} = 1.2$ cm), the numerically calculated island suppression (red curve) is compared with experimental data in Figure 4.2. The results look qualitatively comparable to each other, but the model being used assumes a symmetric temperature perturbation around the resonant radius, r_s whereas the experimental data shows an antisymmetric behavior indicated by the black lines. A possible reason for this behavior observed could be a modification in the magnetic equilibrium in response to the heating well outside the island leading to a further destabilization for $r_{dep} < r_s$ and a further stabilization for $r_{dep} > r_s$ [11]. The results of the radial deposition scan at wide deposition profile ($w_{dep} = 4.6$ cm) is shown in Figure 4.3.

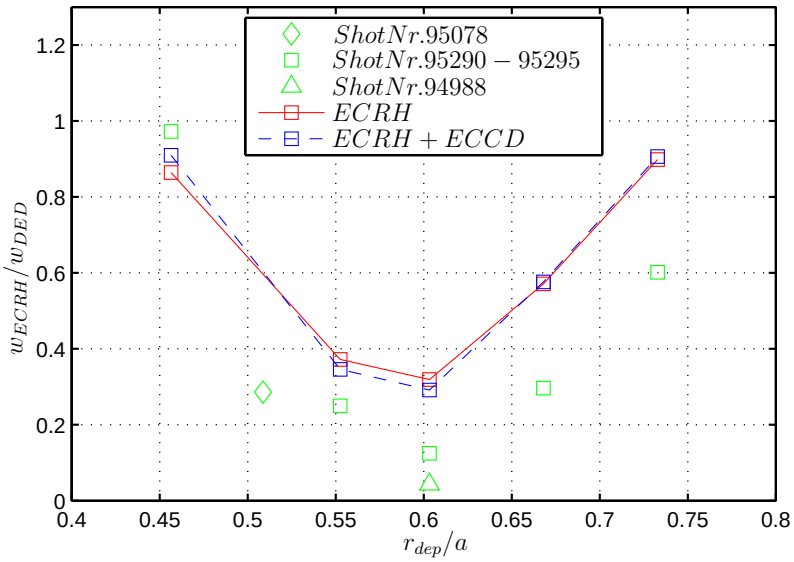

Figure 4.3:
Suppression of the 2/1 magnetic island as a function of radial deposition for wide deposition profile($w_{dep} = 4.6$ cm). Red markers represents the effect of pure ECRH and blue markers represent the effects of both ECRH and ECCD.

As can be seen, there is a negligible influence of ECCD on suppressing the islands. This agrees with the results of these experiments that in TEXTOR the main stabilizing mechanism is ECRH.

When the width of the regions within the effective suppression achieved is compared for two different w_{dep}, it is concluded that wider deposition profiles make sure that at least some power is deposited inside the islands resulting in partial stabilization.

4.3 Comparison concerning the current drive

In this second set of the experiments, by scanning the toroidal injection angle from $\phi = -11°$ to $\phi = +3°$ (positive/negative angles correspond to counter-/co-current drive), the EC driven current has been varied while the vertical injection angle was kept constant. Looking at the experimental results, one can easily see EC driven current has a negligible effect on suppression (see Figure 4.4). Although the values calculated numerically are slightly higher than the experimental results, the fact that there is almost no difference between calculated suppressed island width by ECRH (red markers) and the one by both ECRH and ECCD (blue markers) supports the conclusion drawn above from experiments.

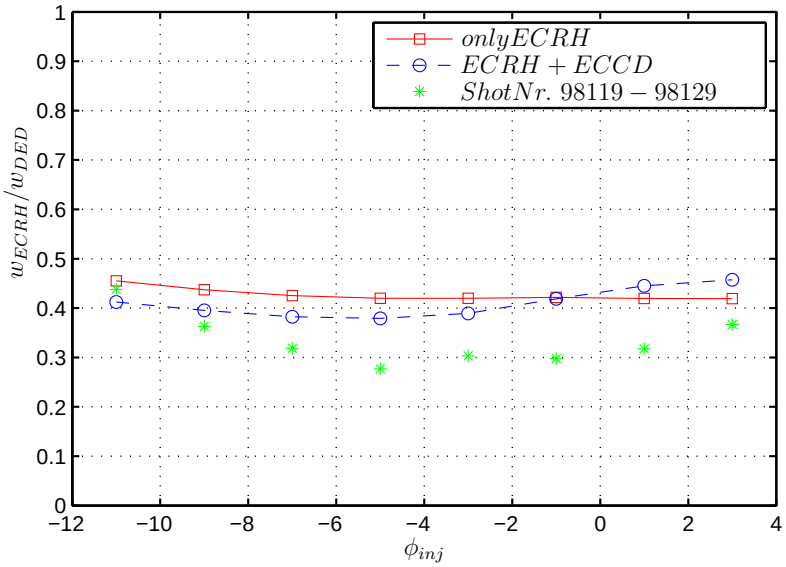

Figure 4.4:
Results of a scan on the toroidal injection angle, ϕ. Green markers show the experimental values while red markers show suppression of islands only by ECRH of power 200 kW and blue markers show the suppression resulting from both ECRH and ECCD.

Note that, while a co-current drive stabilizes the mode, a counter-current drive provides a further destabilization. However, neither in the experimental data nor in numerically calculated values this difference between the effects of counter- and co-current drive on island suppression is significant.

4.4 Comparison concerning the modulation scans

Modulated ECRH experiments were performed by using the current in a DED coil as a reference signal to control the gyrotron power which makes it possible to vary timing and duty-cycle of the high power phase.

4.4.1 Timing scan

The results of timing scan for a fixed duty-cycle (%50) are presented in figure 4.5. Note that the timings for which the center of the high power phase coincides with the passage of the O- or X-point of the magnetic island through the region of power deposition are pointed.

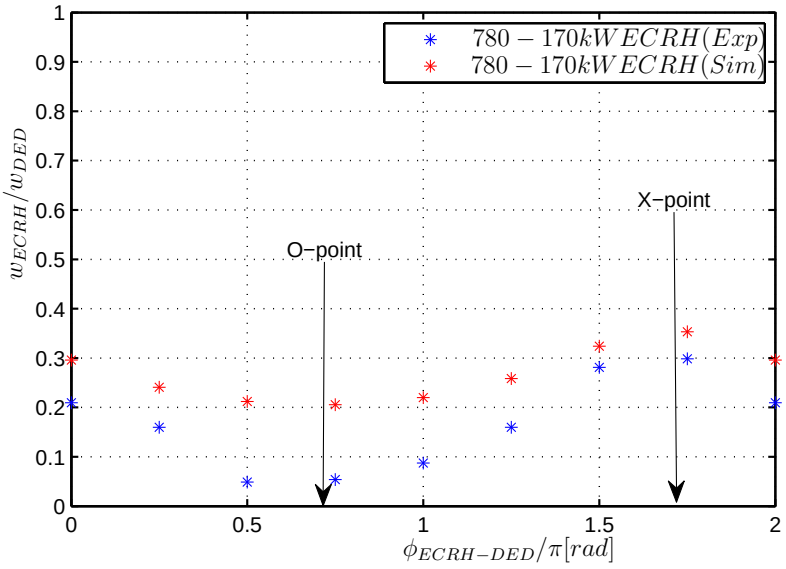

Figure 4.5:
Suppression of the 2/1 magnetic island as a function of the timing of the high power ECRH phase in a modulated ECRH experiment. The horizontal axis gives the phase difference between the start of the ECRH high power phase and the DED current reference signal(taken as a sin-wave). Arrows point the timings for which the ECRH high power phase is centered at either the O- or X-point.

Numerically calculated values follow the same trend as the experimental data, which can be stated as power deposition at the O-point is more efficient

on suppressing the island than deposition at the X-point. However, the difference between the efficiency of O-point heating and the X-point heating in the experimental values is larger than the difference between those in numerical calculation.

4.4.2 Duty-Cycle scan

In the second part of the modulated ECRH experiments, the duty-cycle of a high power phase centered around the O-point passage was scanned (see Figure 4.6).

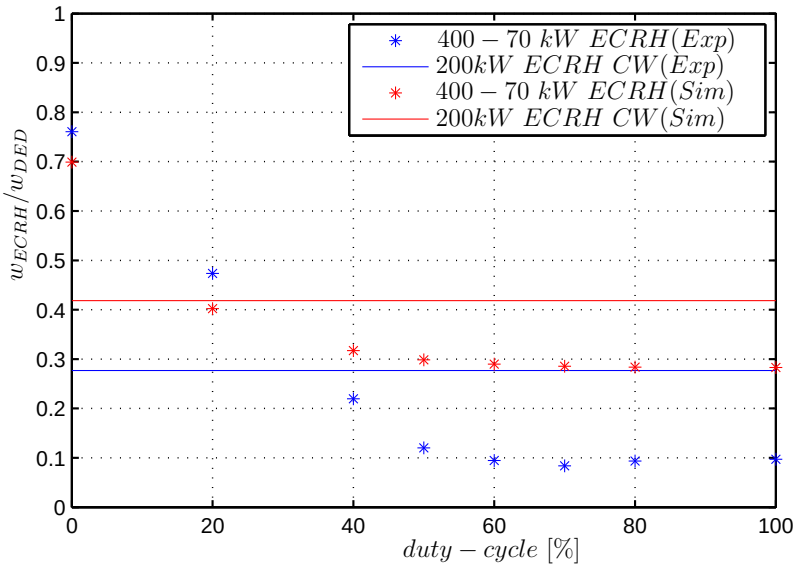

Figure 4.6:
Suppression of the 2/1 magnetic island by modulated ECRH centered around the O-point as a function of the duty cycle of the ECRH high power phase. Red markers show the experimental values and blue markers show numerically calculated suppression of islands.

The modulated power varies between 70 kW and 400 kW, for which the duty cycle corresponds to 0% and 100%, respectively. The efficiency of 200 kW CW power is also compared with the efficiency a modulated power with duty-cycle 40% (which corresponds to same power) has on suppressing the islands. It can be clearly seen that although experimental and numerical results show qualitatively the same trend, their difference grows as experimental data values become smaller. For both cases as duty-cycle is increased, the efficiency also increases but no further improvement is found beyond a duty-cycle of about 60%.

Another common behavior of these two kind of results is that the modulated ECRH with 40% duty-cycle results in further stabilization than CW ECRH at the same average power.

CHAPTER 5

DISCUSSION AND OUTLOOK

This project is focused on a benchmark of the model given in the second chapter with the data of island suppression experiments performed on TEXTOR tokamak. In the third chapter, by comparing the measured temperature profiles [3] inside three fully suppressed magnetic islands (each with a different ECRH input power) with a numerically calculated profile, an approximate perpendicular heat conductivity, $\chi_\perp$ value for each case has been calculated. It is noticed that the difference in the powers deposited does not dramatically affect the value of $\chi_\perp$ inside the island. That is why, an average value ($\chi_\perp = 1.2$ m^2/s) has been chosen to be used for the rest of the TEXTOR simulations. In the fourth chapter, 2/1 magnetic island suppression was simulated and the results were benchmarked with the data of island suppression experiments [17] performed at TEXTOR. Comparisons are based on three different scans. Firstly, comparisons concerning radial deposition scans have been made at narrow deposition profile and at wide deposition profile. The results at narrow deposition profile indicate a further destabilization for $r_{dep} < r_s$ and a further stabilization for $r_{dep} > r_s$. A possible reason might be a modification in magnetic equilibrium because of the heating well outside the island. This modification is not taken into account in deriving the theoretical model. At wide deposition profile numerically calculated suppressed island sizes, one representing the effect of pure ECRH and the other representing the effects of both ECRH and ECCD,

lead to the same conclusion as experimental ones that in TEXTOR heating inside the island is the dominant suppression mechanism. Moreover, it is obvious that wider deposition profile provides a wider region in which stabilization is achieved.

The second set of comparisons have been made concerning the variation in the EC driven current. Calculated island sizes suppressed by pure ECRH and by both ECRH and ECCD are found out to be almost the same. It gives an agreement with conclusion drawn from the experimental data that EC driven current has a negligible contribution to stabilize the islands. Another observation is that neither experimental data nor numerically calculated sizes show a significant difference in the effects of counter- and co-current drive on island stabilization.

The final set of comparisons are concerning the modulation scans composed of timing and duty-cycle scan. Both numerical values and experimental data of the timing scan agrees on that O-point heating is more effective than X-point heating on island suppression. The experimental and numerical values of the duty-cycle scan follow the same trend but as experimental data values become smaller, the difference between them gets larger. Besides both values indicates that the efficiency of modulated ECRH around the O-point on island suppression increases as duty-cycle is increased but no further improvement is observed beyond a duty-cycle of about 60%. The relation between experimentally obtained and numerically calculated w_{DED}/w_{ECRH} for timing scan, duty-cycle scan and rotation scan (current drive) performed has been plotted (see Figure 5.1). Note that the experimental values are found out assuming ΔT is proportional to island width.

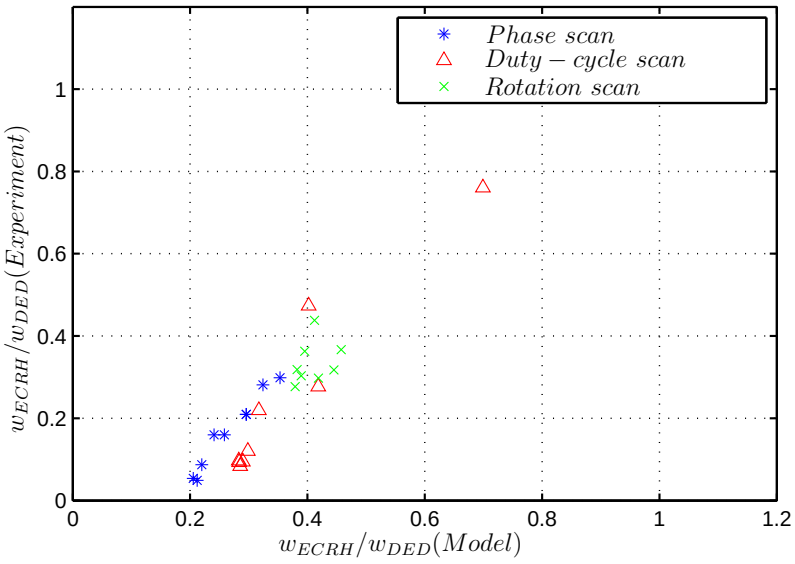

Figure 5.1:
The scattering of experimental island suppression values versus numerically calculated suppression values for timing scan, duty-cycle scan and rotation scan. It is seen that the relation is nonlinear in most of cases.

A better agreement between the model and the experimental data would be possible in case the relation between ΔT and the island size would be non-linear, in particular for small islands. In fact there are also good reasons why this might be the case:

1. As given by the equation 2.36 island width w is proportional to $\sqrt{\psi_1}$ (perturbed flux function).

2. The displacement between the point where temperature is measured and the island is proportional to ψ_1. Thus, ΔT is also proportional to ψ_1.

These arguments would result in an island size w being proportional to $\sqrt{\Delta T}$. For large islands, such that the point of measurement falls inside

the island, the temperature perturbation would still be expected to vary linearly with w.

In order to better assess the validity of the model, further numerical simulations could be performed to obtain a more reliable estimate of the island size from the temperature perturbation. Besides, discharges discussed in [3] could be analyzed to find out the experimental relation between ΔT and w.

REFERENCES

[1] D. Biskamp. *Nonlinear Magnetohydrodynamics*. Cambridge University Press, August 1997.

[2] M. De Bock. *Understanding and controlling plasma rotation in tokamaks*. PhD thesis, Technische Universiteit Eindhoven, 2007.

[3] I. Classen. *Imaging and control of magnetic islands in tokamaks*. PhD thesis, Technische Universiteit Eindhoven, 2007.

[4] K.H. Finken and G.H. Wolf. Background, motivation, concept and scientific aims for building a dynamic ergodic divertor. special issue: Dynamic ergodic divertor. *Fusion Engineering and Design*, 37(3):337–340, 1997.

[5] R. Fitzpatrick. Helical temperature perturbations associated with tearing modes in tokamak plasmas. *Physics of Plasmas*, 2(3):825–838, March 1995.

[6] J. P. Freidberg. Ideal magnetohydrodynamic theory of magnetic fusion systems. *Reviews of Modern Physics*, 54(3):801, July 1982.

[7] J. P. Hans Goedbloed and Stefaan Poedts. *Principles of Magnetohydrodynamics: With Applications to Laboratory and Astrophysical Plasmas*. Cambridge University Press, August 2004.

[8] R.J. La Haye. Neoclassical tearing modes and their control. *Physics of Plasmas*, 13(5), May 2006.

[9] C.C. Hegna and J.D. Callen. On the stabilization of neoclassical magnetohydrodynamic tearing modes using localized current drive or heating. *Physics of Plasmas*, 4(8):2940–2946, August 1997.

[10] D. De Lazzari and E. Westerhof. On the merits of heating and current drive for tearing mode stabilization. *Nuclear Fusion*, 49(7), July 2009.

[11] D. De Lazzari, E. Westerhof, and B. Ayten. On the merits of heating and current drive for tearing mode stabilization. 36^{th} *EPS conference on Contr. Fusion and Plasma Physics, Sofia*, 2009.

[12] J.W. Oosterbeek. *Towards a self-aiming microwave antenna to stabilise fusion plasmas*. PhD thesis, Technische Universiteit Eindhoven, 2009.

[13] P. H. Rutherford. Nonlinear growth of the tearing mode. *Physics of Fluids*, 16(11):1903, 1973.

[14] F. J. B. Salzedas. *The disruptive instability in Tokamak plasmas*. PhD thesis, Utrecht University, 2000.

[15] O. Sauter. On the contribution of local current density to neoclassical tearing mode stability. *Physics of Plasmas*, 11(10):4808–4813, 2004.

[16] J. Wesson. *Tokamaks*. Oxford University Press, USA, 1997.

[17] E. Westerhof, A. Lazaros, E. Farshi, M.R. de Baar, M.F.M. de Bock, I.G.J. Classen, R.J.E. Jaspers, G.M.D. Hogeweij, H.R. Koslowski, A. Kramer-Flecken, Y. Liang, N.J. Lopes Cardozo, and O. Zimmermann. Tearing mode stabilization by electron cyclotron resonance heating demonstrated in the TEXTOR tokamak and the implication for ITER. *Nuclear Fusion*, 47(2):85–90, 2007.

[18] R.R. Weynants. Fusion machines. *Fusion Science and Technology*, 53(2T):37–43, February 2008.

[19] H.R. Wilson. Neoclassical tearing modes. *Fusion Science and Technology*, 53(2T):152–160, February 2008.